INSTITUT DE FRANCE
Académie des sciences

Comptes Rendus

Géoscience

Sciences de la Planète

Catherine Noiriel and François Renard

Four-dimensional X-ray micro-tomography imaging of dynamic processes in geosciences

Volume 354 (2022), p. 255-280

Published online: 12 July 2022

https://doi.org/10.5802/crgeos.137

Les Comptes Rendus. Géoscience — Sciences de la Planète *sont membres du Centre Mersenne pour l'édition scientifique ouverte*
www.centre-mersenne.org
e-ISSN : 1778-7025

Comptes Rendus
Géoscience — Sciences de la Planète
2022, Vol. 354, p. 255-280
https://doi.org/10.5802/crgeos.137

Review Article — Hydrology, hydrogeology

Four-dimensional X-ray micro-tomography imaging of dynamic processes in geosciences

Catherine Noiriel *, [a] **and François Renard** [b, c]

[a] Géosciences Environnement Toulouse, Observatoire Midi-Pyrénées, Université Paul Sabatier, CNRS, IRD, CNES, Université de Toulouse, 14 avenue Edouard Belin, 31400 Toulouse, France

[b] Njord Centre, Departments of Geosciences and Physics, University of Oslo, Norway

[c] ISTerre, Univ. Grenoble Alpes, Grenoble INP, Univ. Savoie Mont Blanc, CNRS, IRD, Univ. Gustave Eiffel, 38000 Grenoble, France

E-mails: catherine.noiriel@univ-tlse3.fr (C. Noiriel), francois.renard@mn.uio.no (F. Renard)

Abstract. The dynamic response of rocks to thermal, hydrodynamical, mechanical, and geochemical solicitations is of fundamental interest in several disciplines of geosciences, including geoengineering, geophysics, rock physics, hydrology, mineralogy, and environmental and soil sciences. From crystal shape to rock microstructure or pore space and fluid distribution, parameters characterizing the rock physico-chemical properties evolve at different time and spatial scales. X-ray micro-tomography (XMT), as a non-invasive and non-destructive imaging technique, offers an unprecedented opportunity to add the fourth dimension, i.e. time, to the three-dimensional spatial visualization of rock and mineral microstructures. The technique is increasingly used to explore dynamic processes in porous and fractured rocks, thanks to synchrotron sources and laboratory XMT scanners, new generations of detectors, and increasing computational power. Image processing allows for tracking the evolution of the fluid–fluid or fluid–mineral interfaces as well as measuring incremental deformations, as rocks deform and react through time under *in situ* conditions of the sub-surface. Here, we review recent advances in 4D X-ray micro-tomography applied to thermo-hydro-mechano-chemical (THMC) sub-surface processes where fluids, porosity, minerals, and rock microstructures evolve together.

Keywords. X-ray micro-tomography, 4D imaging, Mineral reactivity, Reactive flow, Rock deformation, Multi-phase flow, Thermo-hydro-mechano-chemical processes.

Note. Submission by invitation of the editorial board. Catherine Noiriel is the 2020 recipient of the Prix Schlumberger of the Académie des sciences / Soumission sur invitation du comité de rédaction. Catherine Noiriel est la lauréate 2020 du Prix Schlumberger de l'Académie des sciences.

Manuscript received 22 April 2022, accepted 13 June 2022.

* Corresponding author.

1. Introduction

X-ray micro-tomography (XMT) imaging has unraveled the complex structure of many geological materials for 30 years. The technique is based on the attenuation of X-rays crossing a sample, which depends on the X-ray energy and on the atomic composition and density of the material under investigation. The development of XMT relies on three-dimensional (3D) reconstruction of the internal and external structure of a sample from a series of two-dimensional (2D) radiographs taken at different rotation angles. Every voxel in the reconstructed volume represents the linear average X-ray attenuation coefficient $\overline{\mu}_{T(E)}$ of the different phases contained in this volume element. Additional information about the sample mineralogy, chemical composition or phase identification can be obtained by coupling XMT to X-ray diffraction imaging, X-ray fluorescence imaging, dual-energy or spectral imaging near the absorption edge, or by using specific XMT imaging setup like phase-contrast, holotomography or grating interferometry [e.g., Wolf et al., 2017, Suuronen and Sayab, 2018, Sittner et al., 2021, McDonald et al., 2009].

Useful information about the XMT technique and fields of geosciences explored are reviewed in a fruitful and exhaustive list of articles [e.g., Carlson, 2006, Carlson et al., 2003, Van Geet et al., 2001, Cnudde and Boone, 2013, Maire and Withers, 2014, Wildenschild et al., 2002]. Specific reviews are dedicated to pore-scale flow [Blunt et al., 2013, Wildenschild and Sheppard, 2013], reactive transport [Noiriel, 2015], structural geology and rock mechanics [Renard, 2012, Fusseis et al., 2014b], high pressure science [Guignot et al., 2020] and dynamic processes in geologic systems [Marone et al., 2020].

Advances in 3rd generation synchrotron facilities in the 1990's and in laboratory systems more recently have opened and increased the access of the technique to various research domains. In particular, improvements in optics and detectors, and increasing computational power and data storage have initiated the progressive transition from 3D geometry imaging to 4D time-lapse imaging and 4D real-time imaging, also called dynamic imaging or 4D XMT. The sample is imaged repetitively during dynamic processes at discrete time steps that vary according to: (i) the rate of the process, and (ii) the duration necessary to record a set of radiographs. Time-lapse imaging involves imaging at discrete time steps, e.g., hours, days or months, during the process, whereas real-time imaging involves fast and continuous imaging. In the latter case, the time step, ranging from a few seconds to minutes, corresponds to the acquisition duration of the whole set of radiographs. Depending on these constraints, imaging is performed either *in situ* or *ex situ* using specifically designed setups to control flow, temperature, and pressure (see Section 2). Fast tomography imaging provides direct visualization to rapidly evolving or unstable systems, such as flowing fluids (liquid, gas) or reacting components. In addition, it greatly reduces artifacts inherent to motion of fluids [Marone et al., 2017, Villanova et al., 2017] previously encountered. Dynamic acquisition, e.g., high-frequency time-lapse acquisition, involves continuous imaging of the sample, a technique also called X-ray tomoscopy [García-Moreno et al., 2019]. The time lapse between two image acquisitions is limited by the exposure time and the number of radiographs taken, in relation with the sample composition (highly absorbent materials require a longer exposure time) and the desired quality of the reconstructed volume (a lower number of radiographs increases artifacts). For instance, a number of radiographs reduced to a few hundreds can decrease acquisition down to 50 ms [Marone et al., 2017]. The recent upgrade to 4th generation synchrotron facilities with brighter photon beams, such as the Extreme Brilliant Source at the European Synchrotron Radiation Facility [Rack, 2020], offers an unprecedented opportunity for high-frequency time-lapse acquisition in the domain of Digital Rock Physics.

This article focuses on recent developments and applications of time-lapse 4D X-ray microtomography imaging to study dynamic processes in the field of geosciences. We review different applications where visualization through time has unravelled the complex interplay between geochemical reactions, fluid flow, transport, and deformation processes in rocks.

2. Experimental apparatuses

2.1. *Coupling 4D imaging with experiments*

XMT imaging lies in the acquisition of a few hundreds to thousands of radiographs of a sample while rotating on a mechanical stage. The radiographs are used

to generate the sinograms and ultimately the sample absorption 3D map by staking the set of reconstructed 2D slices [Marone et al., 2010, Maire et al., 2001]. The range of rotation angles depends on the X-ray beam characteristics. While the parallel beam generated by synchrotron sources produces a complete set of radiographs over 180°, X-ray tubes in laboratory systems produce divergent X-rays, thus making a 180° plus fan angle rotation compulsory for 3D volume reconstruction. Practically, the set of radiographs is generally produced over 360° on laboratory XMT scanners to get a better signal-to-noise ratio.

XMT imaging is performed either *ex situ* or *in situ*. Several devices, from flow-through cells to rock deformation rigs, have been developed to analyse the response of rock samples to thermo-hydro-bio-mechano-chemical solicitations, with applications ranging from CO_2 sequestration, enhanced oil recovery, and reactive transport, to geomechanics, geological engineering, and geohazards. For *ex situ* imaging, the sample is removed from and replaced in the experimental apparatus and placed on the stage at every imaging step. In that case, the 3D data sets must be registered afterwards, i.e., put in the same coordinate system (see Section 3). A rigid transformation involving translation and rotation along the x–y- and z-directions allows for further image difference and visualization of geometry modifications through time. In contrast, *in situ* imaging requires the whole setup to be placed next to the X-ray beam, while the sample remains positioned on the rotation stage. A few major constraints are identified. First, rotation of the sample and sample holder must be allowed. In some setups, the whole setup is rotated, requiring a high weight-bearing rotation stage. In others, the mobile flow/deformation cell is installed on the sample stage and connected to immobile components set aside, e.g., thanks to slip rings and flexible tubing and connectors. In any case, the setup must not interfere with X-rays, for instance through obliteration of part or totality of the incident beam at certain angles of rotation. Indeed, the presence of absorbent components in the radiographs at discrete angular positions will alter volume reconstruction by producing artifacts. The core holder itself, which also absorbs X-rays, should not reduce much the flux of photons passing through the sample. To increase the photon flux, a white (i.e., polychromatic) beam may be preferred over a monochromatic X-ray source, even if it generates more noise in the images. In some cases, however, the high absorption and filtering properties of the core holder permit to work with a pink beam (i.e., filtered white beam) instead of a white beam in order to obtain a greater photon flux and potentially much faster acquisitions while maintaining a high signal-to-noise ratio.

The size of the sample is intimately related to the imaging resolution, with the sample diameter in most experiments equal to the voxel size times the number of pixels of the camera in the x- or y-direction (about 2500), such that the entire sample fits in the camera field of view. Samples are generally about 1 cm in diameter, thus allowing a good compromise between the voxel size, the spatial resolution of the structures (about 5 μm) and the quest for representative elementary volume (REV) [Bear, 1972]. The voxel-resolution-to-sample-size constraint can be overcome through horizontal or vertical multi-scanning and stitching of the sub-volumes after reconstruction. Local micro-tomography is another option [Baruchel et al., 2000]. In the later case, the sample diameter is larger than the field of view of the camera and a subvolume inside the sample is imaged. The reconstructed image can be affected by artefacts caused by the external parts of the sample whose absorption is recorded in a limited number of radiographs. Multi-scale imaging at different resolutions [Hébert et al., 2015, Peng et al., 2014] can benefit from local tomography to resolve fine structures and derive properties at larger scales, e.g. micro-porosity, in rocks that exhibit heterogeneities spanning several length scales.

The highest spatial resolutions, up to 20 nm voxel size, can be achieved with nano-tomography or X-ray transmission microscopy. In that cases, the X-ray beam is focused ahead of the sample (of size below 1 mm) down to a focal spot that serves as a point source [Withers, 2007].

2.2. *Flow-through cells*

Flow-though cells are designed to explore the response of samples to thermo-hydro-bio-chemical processes in the sub-surface at reservoir conditions, or to quantify the pore-scale distribution of two or more fluids within a sample during drainage and imbibition displacements. The system is generally divided in four parts: (i) a core holder, (ii) a fluid system,

(iii) a set of sensors to measure the fluid and rock properties, and (iv) a data acquisition system to record parameters and control the whole system [Gouze et al., 2017].

Much effort has been done in the past years to design flow-through cells to conduct experiments relevant to *in situ* aquifer and reservoir conditions [Iglauer and Lebedev, 2018] (Figure 1a). Such designs are suitable to reproduce the high pressure and elevated temperatures imposed by the hydrostatic, lithostatic, and geothermal gradients upon sub-surface conditions.

The fluids circulate along the fluid line. One or several pumps control the injection of fluids, and the confining and eventually the axial fluid pressures. The working temperature is reached thanks to a heating system. When no confinement is required, for instance in experiments under atmospheric conditions, mm- to cm-size packed columns are also suitable [Noiriel et al., 2012, Rad et al., 2013, Godinho et al., 2016]. Otherwise, the samples are placed in a core holder and confined to avoid fluid leakage. Reservoir conditions are achieved in high pressure flow-through cells made of materials capable to handle high radial and axial pressures, e.g., aluminum alloy (up to 69 MPa for aviation grade) [Silin et al., 2011, Oren et al., 2019, Herring et al., 2014, Andrew et al., 2014b, Li et al., 2015], carbon fiber [Iglauer et al., 2011], thermoplastic PEEK composite [Saenger et al., 2016], titanium, hastelloy [Luquot and Gouze, 2009] or stainless steel. A set of sensors completes the fluid line or the core holder to record the changes in fluid chemistry and rock physical properties during the experiment. Fluid pressure is generally regulated by back-pressure controllers. Absolute or differential pressure transducers are used to measure the pressure difference between the sample inlet and outlet, which is related to the permeability through Darcy's law [Darcy, 1856]. Linear variable displacement transducers (LVDT) can be added to measure axial strain [Cil et al., 2019].

Fluid characteristics are monitored through online measurements of pH, electrical conductivity or other geophysical parameters [Noiriel et al., 2004, Vialle et al., 2014, Wu et al., 2011]. Recent improvements in online fluid composition determination include Raman spectroscopy probe [Randi et al., 2014]. When fluid composition cannot be assessed directly, fluid samplers allow for sampling under working fluid temperature and pressure, for further determination of pH or/and elemental composition.

Some setups can be mounted directly on the rotation stage for *in situ* imaging during multi-phase flow or tracer injection experiments. Flow may be stopped during scan acquisition to avoid artifacts inherent to the movement of fluids. A first imaging of the sample is generally performed prior to fluid injection, at the pressure conditions of the experiment. This data set is used as the initial reference state prior to experiment and is subtracted from the following 3D volumes.

2.3. *Rock deformation apparatuses*

Rock deformation apparatuses are designed to explore the physical and deformation properties of rocks, e.g., mechanical strength, microstructure evolution, elastic wave velocity and attenuation coefficient in response to earthquake or geomechanical solicitations. However, most rock physics laboratory experiments suffer from major limitations because: (i) direct information about deformation processes inside non-transparent rock samples cannot be obtained without potential unloading artefacts, including fatigue effects and loss of fluid pressure and heat, and (ii) acoustic emission monitoring, which plays the central role in several of these experiments, records only the seismic part of the deformation. Therefore, the time evolution of the 3D deformation field and microstructure geometry inside the samples before and during laboratory earthquakes remain inaccessible. XMT imaging overcomes some of these limitations by simultaneously measuring both the seismic and aseismic components of the rock deformation in well-controlled laboratory experiments. Much effort has been done to design rock deformation apparatuses to conduct experiments at pressure and temperature relevant of the sub-surface *in situ* conditions. The two main limitations of the first XMT experiments were: (i) the flux of photons, which was not high enough to penetrate the thick walls of existing pressure vessels and (ii) the sample environment, of the order of a few kilograms, was too heavy to be carried on the rotation stage. For these reasons, the first dynamic XMT *in situ* experiments on rock materials used portable core holders made of Plexiglas® or glass [Chen et al., 1996, Renard et al., 2004, Viggiani et al., 2004]. Later on, rock deformation apparatuses

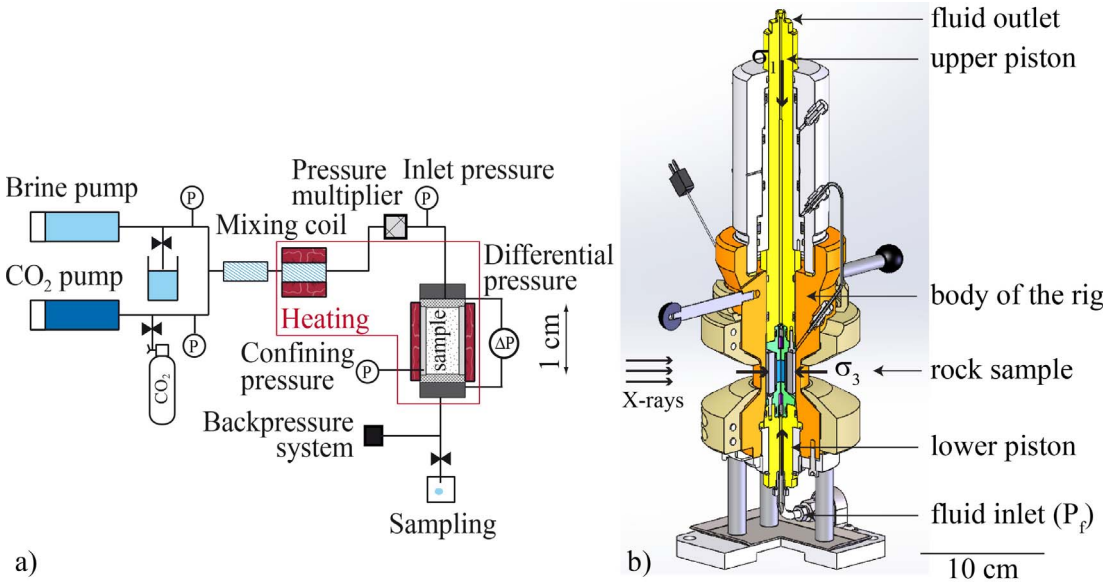

Figure 1. (a) Example of flow-through device to inject fluids at reservoir conditions and desired partial pressures of CO_2 in rock samples; adapted from the setup ICARE [Luquot et al., 2013]. (b) The Hades triaxial rock deformation apparatus developed for *in-situ* imaging [Renard et al., 2016]. The sample is wrapped into a polymer jacket and located between two pistons that impose the axial loading (σ_1). The confining pressure (σ_3) is sustained by oil pressure. Two pumps connected to the fluid line inlet and outlet impose the pore fluid pressure (P_f). The entire body of the rig is heated to the desired temperature.

suitable to *in situ* XMT imaging and that can reproduce pressure and temperature conditions at several meters to few kilometers depth have been built [Hasan and Alshibli, 2012, Fusseis et al., 2014a, Renard et al., 2016, Voltolini et al., 2019, Butler et al., 2020, Cil et al., 2019]. The high X-ray absorption of the core holder, made for instance of titanium [Renard et al., 2016], is overcome by the higher photon flux and sensitivity of the detectors, and by the use of an incident X-ray pink beam instead of a monochromatic beam. The core holders are designed to absorb X-ray wavelengths in a way the X-ray beam crossing the rock sample is about monochromatic. In several triaxial rock deformation apparatuses [Renard et al., 2016, Butler et al., 2020], the confining pressure, axial stress, and pore fluid pressure are controlled independently. These apparatuses use samples of several millimeters in diameter and up to one centimeter in length, such as the Hades apparatus (Figure 1b), which can deform rock samples at conditions of up to 100 MPa confining pressure, 100 MPa pore fluid pressure, 200 MPa axial stress, and temperature of 200 °C. A torsional deformation can also be applied by shearing two rock cylinders separated by a slip surface along which friction occurs [Zhao et al., 2017]. In all these apparatuses, the sample remains in the core holder and the entire setup rotates over at least 180°. For more extreme conditions, the large sample environment around the X-ray transparent gasket does allow for the rotation of the setup, and another technical solution was developed to overcome the possible presence of absorbent components in the field of view. In that case, the high-pressure setup remains fixed, while the sample chamber fully rotates with the top and bottom anvils that pressurize the sample [Wang et al., 2005, Yu et al., 2016]. The weight of the sample assembly neither limits the rotation, nor the small X-ray angular access to the sample. This technology has been applied in the Ultra-fast Tomography Paris–Edinburgh cell (UToPEc) to perform dynamic XMT acquisitions on samples of 8 mm^3 in volume at pressures up to 15 GPa and temperatures of 1000 K [Philippe et al., 2016, Boulard et al., 2018].

3. Four-dimensional image processing

3.1. *Data set registration and image subtraction*

The observation and quantification of microstructure and rock properties evolution in experiments lies on 3D data set comparison through time. To do this, the successive XMT volumes must be registered in the same coordinate system. Registration is required when the sample has been removed from the rotation stage between two imaging experiments (*ex situ* imaging) or when misalignment is observed during *in situ* experiments. It constitutes a crucial step in image processing to compare data sets with each other [Wildenschild and Sheppard, 2013].

Registration is not mandatory for *in situ* imaging, where the sample remains fixed on the rotation stage during the whole experiment and returns to its initial position after acquisition. *In situ* acquisition is preferred for experiments involving mechanical deformation, as sample deformation would make difficult non-rigid registration. When the sample is fixed, it becomes possible to calculate the displacement and deformation fields using for instance digital volume correlation (DVC) (see further in Section 3).

In absence of mechanical deformation, registration consists of a rigid body transformation involving three translations and three rotations along and around the *-x*, *-y*, and *-z* axes. The coefficients of the (4×4) transformation matrix are determined from identification of at least three landmarks in the different volumes. Alternatively, more optimized algorithms based on image intensity distribution, image structure or neuronal network [Maes et al., 1997, Zitová and Flusser, 2003] have been developed to optimize a similarity measure in between two volumes, e.g., mutual information, invariant moments or cross-correlation. Depending on the sample geometry and its evolution through time, one technique is preferred over another to determine the transformation matrix.

Registration starts with a reference volume, generally the initial data set. Sometimes, a given volume at time t_i serves as reference and the following one at t_{i+1} is registered thanks to this reference. The transformation matrix is applied to the volumes to be registered, followed by interpolation of the greyscale intensity of translated and rotated voxels. Resampling of the voxel intensity through a linear interpolation among the neighbour voxels in the new coordinate system is common, although more complex algorithms like cubic or Lanczos resampling exist [Duchon, 1979].

Once registration is achieved, one-to-one comparison of 3D greyscale volumes may involve image normalization, i.e., rescaling of the histograms so that a given material in the sample, e.g., air or a rock element, will have the same distribution of intensities in every volume (Figure 2). Normalization also improves image visualization by adjusting the contrast through scaling of the range of intensity values. Additional denoising of the data sets with 3D median or non-local means filters is also common [Buades et al., 2005].

After these steps, one often proceeds to data set segmentation to assign the different solid and fluid phases in the sample a unique label, e.g., 0 for air, 1 for solid, 2 for liquid.

3.2. *Data set segmentation and field representation*

Segmentation is an essential step for locating the different materials and extracting parameters characterizing the samples, like the volume occupied by the different phases, the position of the interface between two phases, or the phase connectivity and network properties. In addition, digitization of the pore space and rock matrix is necessary to perform direct simulations of flow or mechanical deformation of the solid. Segmentation of XMT volumes is often based on the image intensity distribution, but can possibly be combined with morphological criterion [Meyer and Beucher, 1990]. The simplest way to separate two phases is to select a threshold in the greyscale histogram. However, simple thresholding often fails to properly distinguish in between phases. Indeed, noise inherent to XMT does not imply a single greyscale intensity for a given phase, but rather a distribution of intensities that generally overlap with others and follow Poisson distributions [Cnudde and Boone, 2013]. In this case, more complex algorithms like anisotropic diffusion filters are more suitable. Watershed segmentation based on region-growing is also efficient to ignore the overlaps in the modes characterizing the greyscale histogram. More recently, segmentation based on machine learning has emerged, e.g., convolutional neural networks. From supervised algorithms in which

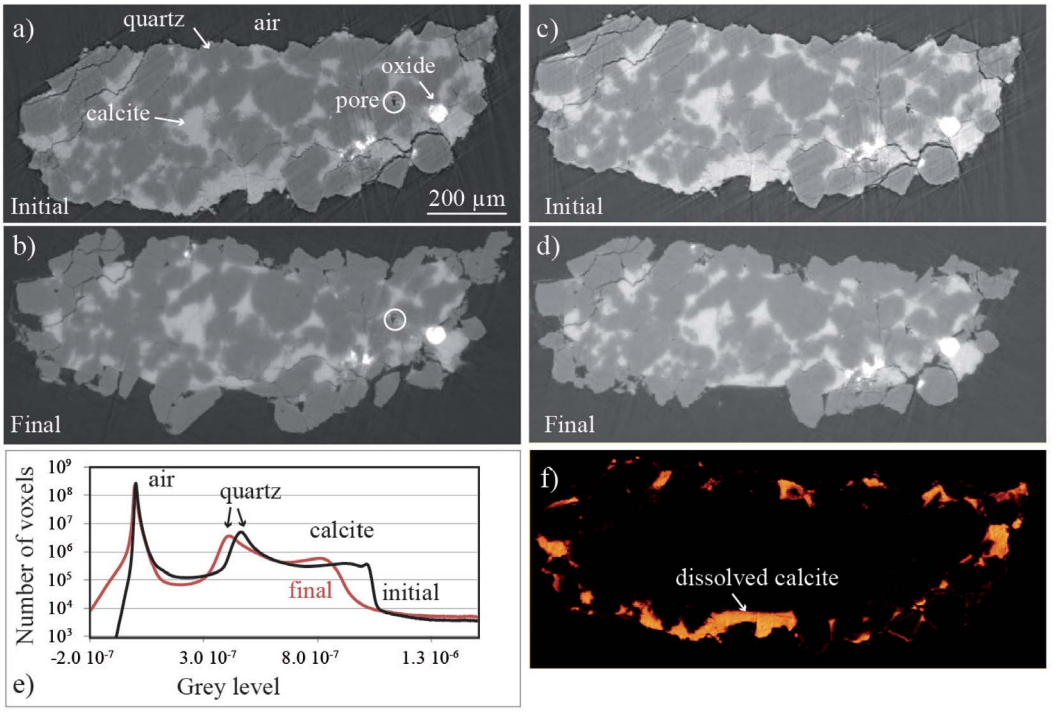

Figure 2. Example of a sandstone sample at two stages of a dissolution experiment at pH 5.5. Cross sections (a,b) before and (c,d) after image registration and normalization; the white circles correspond to a common pattern in the two images. (e) Corresponding histograms of the initial data sets are also shown, showing that the peaks for quartz and calcite are not superimposed. (f) Image difference (initial-final) after image registration and normalization showing the sample geometry evolution, including dissolution of the carbonate cement and disaggregation of some quartz grains.

training features are combined to identified regions of interest in the original image [Arganda-Carreras et al., 2017], to unsupervised algorithms that do not require any training images or ground true labelling of voxels [Kim et al., 2020], several methods can be explored to produce voxel-based segmentation.

3.3. *Interface tracking*

XMT offers the opportunity to resolve fluid–fluid, fluid–mineral and mineral–mineral interfaces, which are key elements in multi-phase flow or geochemical processes occurring at the sub-surface. When the absorption contrast between two phases of close density is too small to be detected, phase contrast XMT can be used to enhance the boundary between the two phases in contact [Cloetens et al., 1996]. After segmentation and labelling of the different phases, identification and tracking of the interface motion becomes possible. The different methods to extract and represent the interface displacement from XMT volumes as their limitations are described in Noiriel and Soulaine [2021]. Under flow or reactive conditions, fluid–fluid or fluid–mineral interface shift can be directly linked to the rate of fluid displacement or the amount of solid removed or precipitated by reactive fluids. The velocity of the interface shift is defined as:

$$v_{\text{int}} = \frac{\mathrm{d}\boldsymbol{I}_{\boldsymbol{fs}} \cdot \boldsymbol{n}}{\mathrm{d}t}, \tag{1}$$

where $\boldsymbol{I}_{\text{int}}$ is the position vector of the interface, and $\boldsymbol{n}$ the normal vector to the interface; the product $\mathrm{d}\boldsymbol{I}_{\text{int}} \cdot \boldsymbol{n}$ is the surface displacement, i.e., the distance normal to the interface.

If evaluation of the motion of sharp, relatively flat interfaces from 3D data sets does not pose a serious problem, it is far more complicated to deal with curved or smeared (i.e. diffuse) interfaces

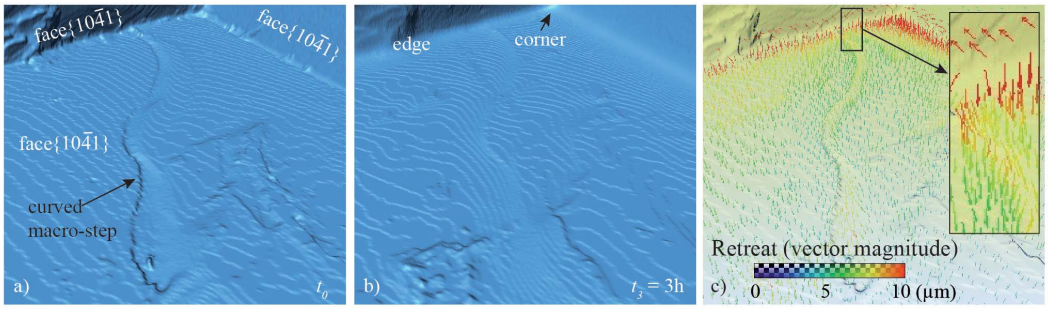

Figure 3. Example of interface tracking during dissolution of a calcite crystal. (a,b) Internal views of the crystal at two time steps (initial and after 3 h of experiment); the solid is transparent and the mineral–fluid interface is in blue color. (c) Mapping of displacement vectors normal to the surface at t_0.

[Noiriel and Soulaine, 2021]. Evaluation of the displacement between two time steps lies in the calculation of the distance between two surfaces, i.e., the interface at times t_i and t_{i+1} (Figure 3a). From the 3D interface discrete geometry derived from XMT, the vectors normal to the reference surface S(t_i) are calculated, then normal rays are projected until they intercept the second surface S(t_{i+1}). The choice of the reference surface is important as propagation distances and directions depend intimately on the curvature of the interface [Sethian, 1999].

In addition, the recession of an interface up to its complete disappearance (e.g., full mineral dissolution), the formation of a new interface (e.g., gas bubble nucleation), the displacement of a closed surface (e.g., solid particle), or the splitting of a given phase volume (e.g., oil ganglia formation) are examples that illustrate the difficulty for tracking some types of interfaces through time. In multi-phase fluid flow, especially, tracking the interface may be difficult because of the large number of interfaces and the large amount of deformation they experience. In that case, tomographic X-ray particle tracking velocimetry [Dubsky et al., 2012, Mäkiharju et al., 2021] techniques may be preferred to measure the fluid velocity and characterize flow more efficiently than XMT.

3.4. *Digital volume correlation*

Time-lapse XMT imaging produces series of volumes whose geometry may evolve with time due to deformation. Techniques have been developed to analyze the incremental strain between successive imaging experiments. When the deformation is large enough, for example when fractures form or pores collapse, a simple visualization and segmentation of the porosity or fracture voids makes it possible the quantification of volumetric strain in crystalline and porous rocks [Renard et al., 2018, Huang et al., 2019, Cartwright-Taylor et al., 2020]. However, in many experiments strain may be locally very small, and the local displacements are smaller than the voxel size.

In this case, digital volume correlation allows for calculation of the local displacements in pairs of images (Figure 4), which comprise a reference image and a deformed image [Bay et al., 1999, Lenoir et al., 2007, Hall et al., 2010]. The deformation field is obtained by optimizing a cross-correlation or a least-squares function that maximizes the matching accuracy between the grey scale intensity values of sub-volumes taken in the two images. Sub-volumes are typically of the order of $10 \times 10 \times 10$ voxels or larger, such that they contain enough information about the sample microstructure, and the contrast for volume correlation is maximized. By identifying similar patterns across pairs of volumes, digital volume correlation produces three-dimensional incremental displacement fields from which the six independent components of the second rank three-dimensional incremental strain tensor may be calculated. These incremental strain fields reveal strain localization that occurred during the time interval between two imaging acquisitions. The calculation of the incremental displacement field is performed at the sub-voxel scale, typically in the range 0.01–0.001 voxel size.

To characterize the resolution of strain values obtained from digital volume correlation analysis, and

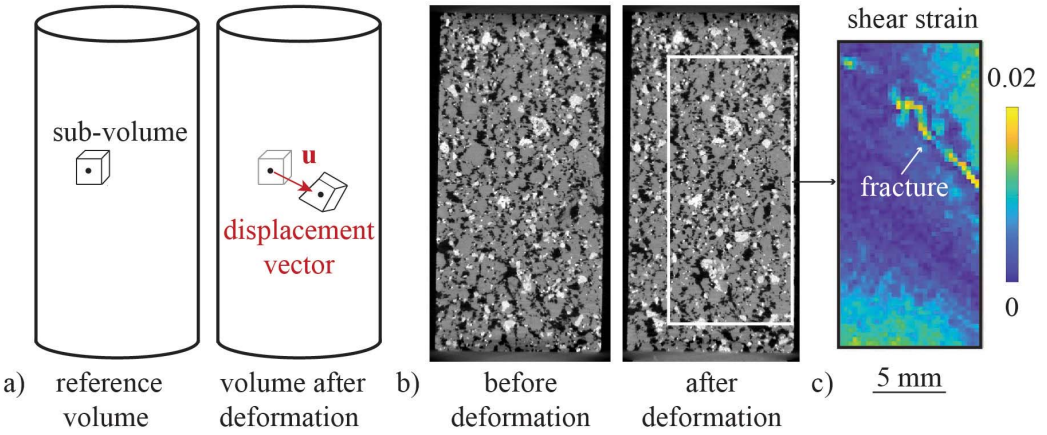

Figure 4. (a) Concept of digital volume correlation where a pair of XMT images is used to calculate the incremental strain. The reference image is divided into subvolumes which are identified in the deformed image. The translation vector u and the strain corresponding to the deformation of the subvolume are calculated. (b) Two images of a porous andesite rock before and after deformation, and (c) resulting identification of a shear fracture with sub-voxel displacement. Adapted from Heap et al. [2020].

thus the lower limit of robust strain values, digital correlation analyses can be performed on the same volume (i.e., auto-correlation), or using two data sets for which the user expects no significant geometry changes (i.e., no strain), for example by imaging the same sample twice without changing the experimental conditions. The incremental strain field can be resolved with a strain resolution in the range 10^{-4}–10^{-1}, depending on the quality of the images. Other quantities may also be calculated, such as the divergence and the curl of the displacement field, the invariants of the strain tensor and the evolution of strain populations within a sample [Renard et al., 2019a], including recent developments based on machine learning techniques to unravel statistical correlations in the data sets [McBeck et al., 2020]. Several digital volume correlation open source codes are available to the scientific community [Tudisco et al., 2017, Yang et al., 2020a].

4. Applications to thermo-hydro-mechano-chemical processes

In the following sections, a brief overview of applications of 4D XMT in geosciences is given, with a specific focus on thermo, hydrodynamical, mechanical and/or chemical coupled (THMC) processes in the sub-surface.

4.1. *Fluid flow and multi-phase flow*

Flow in consolidated and unconsolidated porous media is a field that benefited a lot from XMT imaging, since the pioneering works of Spanne et al. [1994] and Coles et al. [1998] to extract the topology of the porous network and fluid-filled pore space following the displacement of oil by water. Since, an increasing number of multi-phase flow and gas trapping experiments during imbibition or drainage have been performed after doping fluids with contrast agents. Multiphase flow is central to a wide range of geological, industrial and environmental processes, including enhanced oil recovery, CO_2 storage in geological reservoirs, water infiltration in soils, and groundwater contamination by non-aqueous phase liquid (NAPL) [Wildenschild and Sheppard, 2013]. The first time-lapse images of fluid distribution were acquired with CT scanners [Vinegar and Wellington, 1987, Wang et al., 1984] with a spatial resolution, however, insufficient to describe fluid partitioning within the pore space. In contrast, XMT imaging provides information at the pore scale. While the first XMT studies have limited themselves to about two sets of observations since fluid flow generates motion artifacts during acquisition [Culligan et al., 2004, Seright et al., 2002, Wildenschild et al., 2002, Turner et al., 2004], fast X-ray micro-tomography now allows

for direct visualization of moving fluids in course of imbibition or drainage [Berg et al., 2013, Bartels et al., 2019]. In the studies, the dry or fully saturated sample is generally imaged first and then compared with time-lapse data sets showing the fluid distribution in the pore space.

Extensive experimental efforts have been put forward to relate the saturation and relative permeability curves during imbibition or drainage to pore-scale visualization of the fluid distribution [Porter et al., 2010]. Visualization provides all the information to unravel the complex interplay between the effects of capillarity, wetting, and viscous instability within the heterogeneous pore network. Compared to transparent micro-models developed to study multi-phase flow, XMT offers the possibility to work with real rock samples, whose pore space is often heterogeneous at many scales, from peloid or intraclast micro-pores, grain boundaries or clay fraction, to cm-scale vugs or large-scale fractures. Distribution of fluids between the rock micro- and macro-porosity can be quantified [Boone et al., 2014]. In addition, micro-models are unable to reproduce the complex fluid–rock interface properties, the wettability of mineral surfaces being an important factor governing the flow and trapping of the different fluid phases, e.g., water, oil or CO_2.

Time-lapse imaging gives new insights in the dynamics of the fluid phases, including thin films formation, capillary trapping, fluid–fluid interface motion, interfacial curvature, Haines jump, occurrence of snap-off at the pore throats with formation of isolated ganglia, and pinch off and merging of interfaces [Brusseau et al., 2008, Reynolds et al., 2017, Voltolini and Ajo-Franklin, 2019, Scanziani et al., 2018, Lin et al., 2018, Scanziani et al., 2020, Alhosani et al., 2020, Spurin et al., 2020, Alhosani et al., 2021, Kim et al., 2022]. Contact angles, which are important indicators of the wetting characteristics of a fluid-solid interface, can also be determined [Andrew et al., 2014b, Scanziani et al., 2017]. Measurements show a certain variability, explained by contact angle hysteresis during wetting phase advance or recession, and by grain surfaces of variable roughness.

The physics of capillary trapping can also be assessed. In the context of CO_2 sequestration, the entrapment of a non-wetting phase through ganglia formation helps to immobilize CO_2 in the pore space [Iglauer et al., 2011, Zuo et al., 2017], whereas it is detrimental to hydrocarbon production in the context of enhanced oil recovery. Snap-off occurs when a non-wetting fluid displaces a wetting fluid in pore-throat constrictions (Figure 5), leading to the breakup of droplets and formation of ganglia [Berg et al., 2013, Andrew et al., 2014a, Rucker et al., 2021, Singh et al., 2017, Tanino and Blunt, 2012, Scanziani et al., 2020].

Minimization of the entrapment and enhancement of oil mobilization during enhanced oil recovery is possible thanks to a reduction of the capillary forces, through a decrease of the interfacial tension and alteration of the wettability. With this regards, the effect of low-salinity flooding or additives, e.g., polymers, surfactants or nanoparticles, to reverse the wettability of mineral surface from oil-wet to water-wet has been evaluated [Unsal et al., 2019, Singh et al., 2016, Rane et al., 2021, She et al., 2021, Javanbakht et al., 2017, Pak et al., 2018, Qin et al., 2020, Andrews et al., 2021]. The effect of gas injection, i.e., three-phase flow in either immiscible or near-miscible gas conditions has also been assessed [Alhosani et al., 2019]. The techniques can also apply to the *in situ* remediation of contaminated groundwater by NAPL [Pak et al., 2020]. Multi-phase flow has also been studied in fracture networks and the effects of fracture morphology on the distribution and transport of immiscible fluid phases has been investigated [Karpyn et al., 2007, Van Stappen et al., 2018]. More extreme conditions, with a case study relevant to magma migration in the Earth's mantle deserves to be mentioned [Giovenco et al., 2021].

Fast X-ray micro-tomography has also benefited to tracer or colloid injection experiments in transient flow conditions [Bultreys et al., 2016, Van Offenwert et al., 2019, Molnar et al., 2015, 2016], complementary to larger scale studies of diffusive [Polak et al., 2003] or advective–dispersive transport that involved 3D imaging [Boon et al., 2016, 2017]. The experiments are based on the addition of a contrast agent in the tracer, e.g., iodine-rich brine or silver nanoparticles, compared to the fluid used initially to saturate the sample. First, calibration is performed by saturating and imaging the sample with the tracer at different concentrations, in order to correlate the tracer concentration to the grey level in the pore space. To alleviate random noise inherent to XMT, Van Offenwert et al. [2019] decomposed the pore space into individual pore bodies, then averaged the grey level

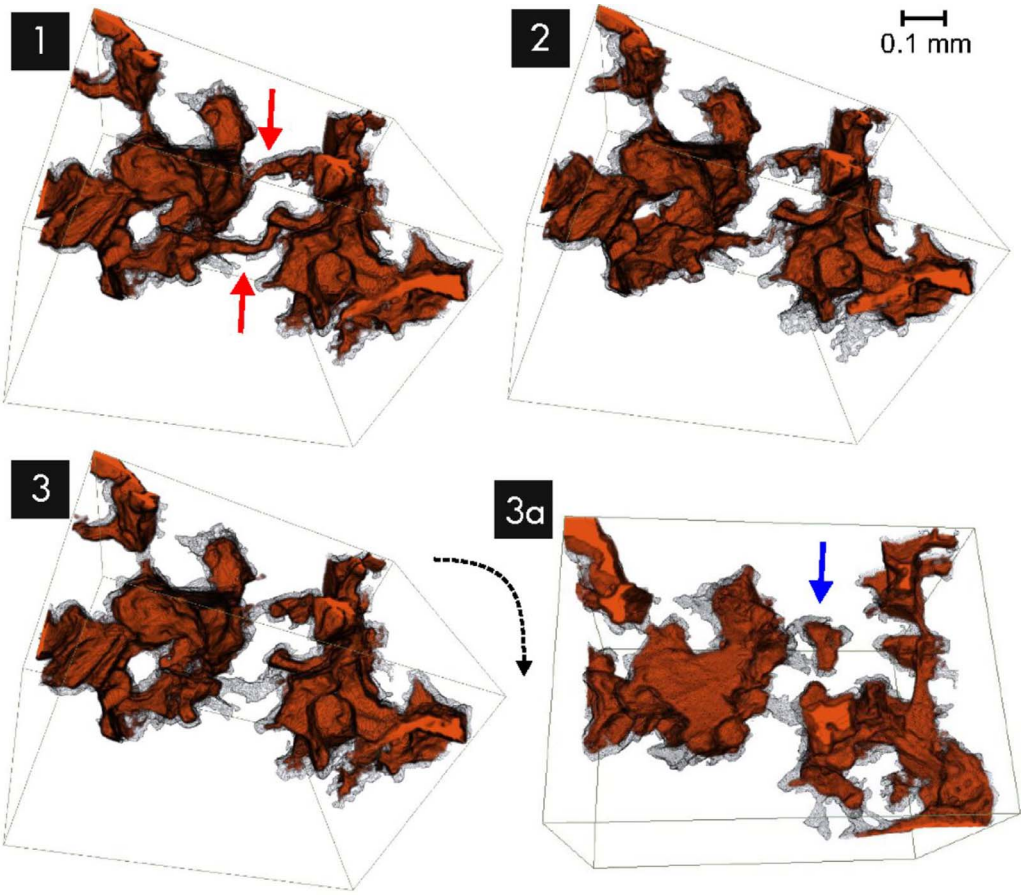

Figure 5. Visualisation of multi-phase flow in porous media at three different time steps (1 to 3), where snap-off events at narrow pore throats (red arrows) promote oil trapping (blue arrow) during imbibition; the solid is transparent and the oil phase is in orange-brown color. Reprinted from [Berg et al., 2013]. (Used with permission of PNAS, from Berg et al. [2013], Figure 5.)

over each pore body to retrieve the tracer arrival time and filling time through the porous network.

4.2. *Mineral reactivity*

XMT-based studies on mineral reactivity are emerging. They have focused on the reactivity of single crystals and minerals, or have explored coupled dissolution/precipitation processes or phase transformation in rocks and rock aggregates. XMT makes possible a detailed description of pore-scale fluid interface dynamics at the sub-micrometer scale (Figure 6), which is complementary to mass balance evaluation, atomic- or nanometer-scale evaluation of the interfacial properties, or numerical approaches using for instance a Kinetic Monte Carlo (KMC) model [Kurganskaya and Luttge, 2016].

Pure diffusion or uniform flow field is assumed near the fluid–mineral interface, so that flow and transport effects can be decoupled from the intrinsic mineral reactivity. The density and the size of nuclei can be resolved in precipitation experiments [Yuan et al., 2021]. From image subtraction during crystal dissolution [Noiriel et al., 2019, 2020, Yuan et al., 2019], it becomes possible to calculate and map the retreat at the crystal surface, as well as the local reaction rate at any surface element, i.e., any pixel at the fluid–crystal interface (see for instance Noiriel et al. [2020] for more details about the procedure). The technique is complementary to classical

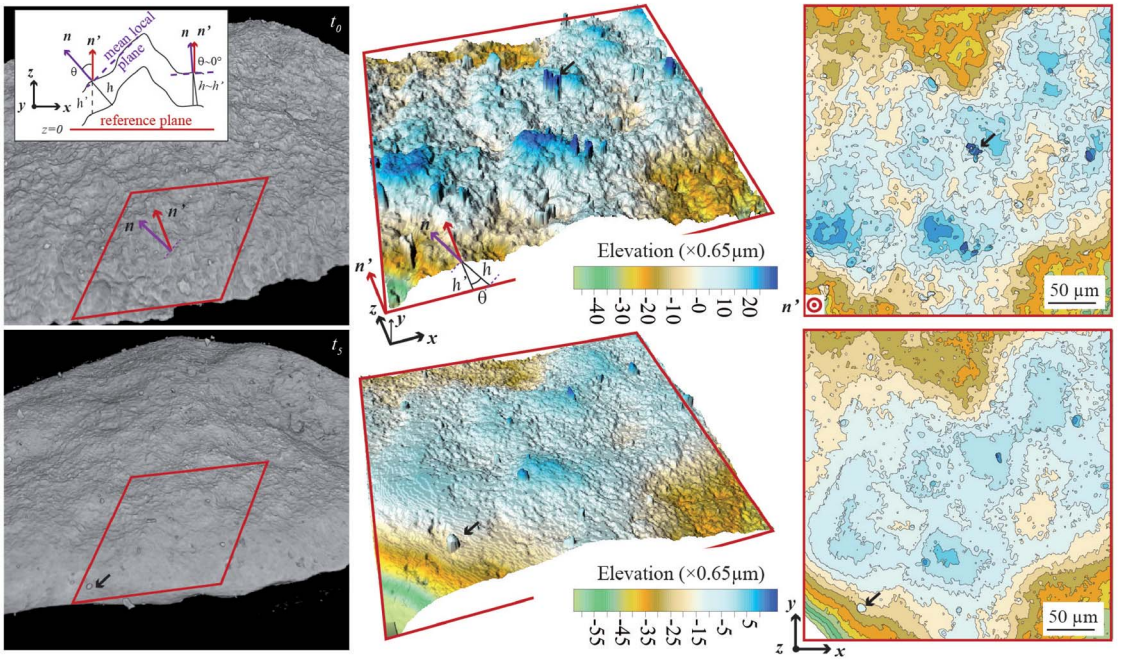

Figure 6. Visualisation of the fluid–mineral interface displacement during dissolution of a limestone aggregate at pH 4. The red square is 512×512 pixels in size, and the interface roughness is observed to decrease with time. Reprinted from Noiriel and Soulaine [2021]. (Used with permission of Springer, from Noiriel and Soulaine [2021], Figure 2).

methods measuring the surface retreat, e.g., atomic force microscopy (AFM) or vertical scanning interferometry (VSI) and extends the measurements in the third dimension. Therefore, it provides the dissolution rate distribution for a whole crystal, thanks to the unlimited depth of investigation of XMT. For instance, it is particularly suitable to investigate calcite dissolution under acidic conditions [Noiriel et al., 2019, 2020, Yuan et al., 2019], where dissolution is enhanced at the crystal corners and edges compared to the flat crystal faces, or to evaluate the poisoning effects of Pb^{2+} on the crystal morphology evolution and rate distribution [Yuan et al., 2019].

Leaching experiments of cementitious materials [Burlion et al., 2006, Rougelot et al., 2009, Bossa et al., 2015] or ore particles [Kodali et al., 2011, Gao et al., 2021, Eckley and Ketcham, 2019, Ram et al., 2020, Lo et al., 2016] have also benefited of XMT imaging to explore the porous network structure evolution, derive rates at which these processes occurs, and in the latter case determine the extent of valuable mineral recovery.

XMT has also revealed the complex interplay during dissolution/precipitation coupled reactions or phase transformation, which are explored using either single crystals [Kim et al., 2021] or aggregates confined in pressure vessel. For example, Fusseis et al. [2012] and Bedford et al. [2017] have provided insights in the dehydration reactions during heating of gypsum ($CaSO_4$, $2H_2O$) and subsequent transformation into bassanite ($CaSO_4$, $0.5H_2O$), whereas Zheng et al. [2017] have investigated the hydration of periclase (MgO) into brucite ($Mg(OH)_2$). Carbonation of olivine in the context of CO_2 sequestration has also been explored [Zhu et al., 2016, Xing et al., 2018]. Especially, XMT is suitable to follow reaction fronts and evaluate the volumetric variations associated to these processes, e.g., creation or destruction of porosity.

4.3. *Reactive flow*

Mineral reactivity involves changes in the pore space architecture, thus affecting the flow and transport

properties along the flow paths (Figure 7). The flow-through core holders described in Section 2 are useful setups for coupling visual examination of the rock geometry evolution to measurements of physico-chemical parameters like porosity, permeability, dispersivity or reaction rates. The first studies that benefited from 4D XMT focused on single-phase reactive flow experiments for modeling permeability evolution as a function of porosity, 3D pore geometry, and fluid–rock interface reactivity [Noiriel et al., 2005, Bernard et al., 2005]. Modelling of the flow and transport properties, as upscaling from the pore scale to the Darcy's scale is another challenge linked to reactive flow experiments [Noiriel et al., 2012].

A specific attention has been paid over the last 20 years to the study of the fate of CO_2 in porous and fractured rocks. Dissolution of $CO_{2(g)}$ into water, by acidifying aqueous fluids, should promote mineral dissolution near the injection wells, while precipitation of carbonated phases is expected further in the reservoir following the release of chemical elements and supersaturation with respect to carbonate minerals. Many experiments have been performed at different pressures, temperatures, partial pressures of $CO_{2(g)}$ and fluid compositions in various reservoir and cap rocks, including limestone, dolostone, sandstone, basalt, and shale. The impact of mineral reactivity to the porosity–permeability curves has been explored in relationship with microstructual modifications [Noiriel et al., 2004, 2005, Qajar and Arns, 2022] or with the Péclet and Damkhöler numbers [Luquot and Gouze, 2009, Noiriel et al., 2013, Menke et al., 2015, 2017a, 2018, Al-Khulaifi et al., 2017, 2018], two parameters that weight the relative contribution of advective to diffusive transport, and of the chemical reactions to transport, respectively.

The formation of preferential flow paths, from conical to highly ramified wormholes [Golfier et al., 2002] is not solely a function of the Péclet and Damkhöler numbers, and studies have also emphasized the geometry and the mineral or structural control of reservoir rock on the development of reaction fronts [Luquot and Gouze, 2009, Smith et al., 2013, Luquot et al., 2014, Garcia-Rio et al., 2014, Qajar and Arns, 2017b,a, Al-Khulaifi et al., 2019, Privalov et al., 2019, Menke et al., 2017b, Yang et al., 2020b, Leger et al., 2022]. Heterogeneities arise both from the pore space structure and from the chemical and mineralogical distribution of the solid phases. In particular, the rock textures combining highly reactive minerals (e.g., sulfates, carbonates) to low reactive minerals (e.g., silicates) promote unexpected behaviours during dissolution processes, like permeability reduction despite net dissolution [Gouze et al., 2003, Noiriel et al., 2007b,a, Ellis et al., 2013, Spokas et al., 2019].

Alteration of silicates, through of the release of cations (Ca^{2+}, Mg^{2+}, Fe^{2+}) can promote precipitation when solution becomes supersaturated with respect to other mineral phases. Precipitation can be very local, homogeneous or highly heterogeneous at the pore scale depending of the fluid composition evolution within pores, and on the mineral surface energy for nucleation and growth [Noiriel et al., 2016]. Besides, the dynamics nature of crystal growth and mineral precipitation has been investigated in porous columns packed with glass beads and carbonates mimicking analogues of sandstone and limestone [Noiriel et al., 2012, 2016, Godinho et al., 2016, Godinho and Withers, 2018], examining the role of bacteria-induced mineral precipitation [Wu et al., 2011]. Fractures have also been investigated to explore the role of precipitation on the reorganization of flow and transport [Menefee et al., 2020, Noiriel et al., 2021].

Soil physics and cultural heritage studies have also benefited from 4D XMT imaging. The effects of salinity on the evaporation rates in granular porous media [Rad et al., 2013], the pore structure change or the cracking dynamics and clay desiccation have been assessed [Keyes et al., 2016, 2017, DeCarlo and Shokri, 2014, Dewanckele et al., 2012]. The studies have also pointed to the role of heterogeneities on transport and reactions processes. Thermal effects, studied through freeze–thaw cycling, permit to better link the crystallization-induced stress to the amount of pores filled by crystals [De Kock et al., 2015]. In most of the studies, mechano-coupling is also involved in the reactive flow processes.

4.4. *Rock deformation and mechano-chemical coupling*

Rock deformation experiments that use 4D imaging have opened a new era in rock physics and geomechanics to improve our knowledge of fluid-mediated

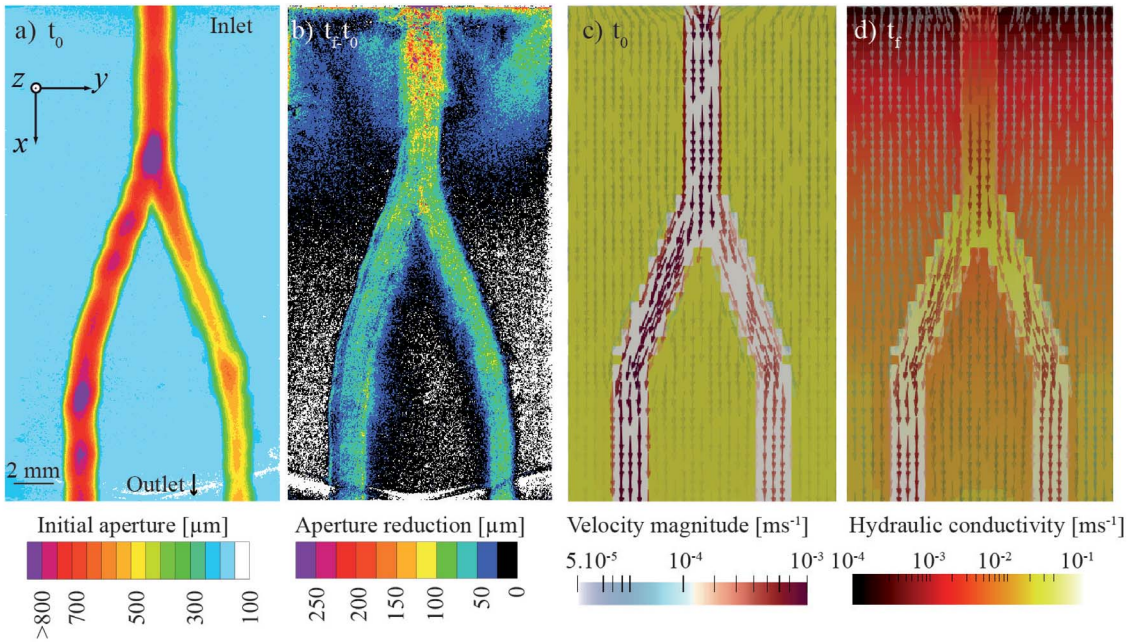

Figure 7. Visualisation of preferential precipitation of calcite in the main flowpaths of an artificial fracture grooved with two channels. The rock is a dolomitic limestone. (a) Initial aperture field derived from XMT; the sample was 50 mm in length and only the part close to the inlet is shown. (b) Aperture reduction after 16.7 days of reactive flow. Modelling of reactive flow in a model fracture geometry shows evolution of the fluid velocity (arrows) and local permeability (background color) between initial (t_0) and final (t_f) time. For more information about the experiment and modelling of reactive transport, see Noiriel et al. [2021].

and stress-controlled deformation mechanisms [Renard et al., 2004, Viggiani et al., 2004, Gratier et al., 2015, Macente et al., 2019]. With the development of triaxial deformation apparatuses installed on synchrotron beamlines, it is now possible to analyze several important geomechanical and geophysical processes. For example, the growth of microfractures prior to system-size failure in crystalline rocks are identified as an important process during the preparation phase of laboratory earthquakes (Figure 8). The evolution of the microfracture network when approaching failure was described as a critical phase transition [Renard et al., 2018, Cartwright-Taylor et al., 2020], characterized by a competition between dilation, compaction, and left-lateral and right-lateral shear [Renard et al., 2019b].

The impact of fluids on pore pressure buildup and rock damages, either fluids released from dehydration reactions [Marti et al., 2021] or fluids promoting hydration reactions [Voltolini and Ajo-Franklin, 2020] have also been investigated.

In reservoir geology, how porosity evolves during reservoir compaction, shale maturation, and formation of faults controls permeability. These topics are highly relevant for hydrocarbon exploration, carbon dioxide or nuclear waste storage, and more generally transport of fluids in geological reservoirs and caprocks. XMT experiments have quantified the mechanisms of strain localization in porous sand and sandstones [Louis et al., 2007, Hall et al., 2010, Renard et al., 2019a], limestones [Huang et al., 2019], and shales [Lenoir et al., 2007, McBeck et al., 2018, Voltolini and Ajo-Franklin, 2020, Voltolini et al., 2017]. Shale maturation was reproduced under *in situ* conditions to demonstrate that the heating of kerogen leads to the formation of microfractures and fluid expulsion. The mechanism that couples thermal, hydraulic, and brittle deformation processes controls the primary migration of hydrocarbon from the source rocks to the reservoir [Tissot et al., 1987] is now accessible using 4D XMT imaging [Kobchenko et al., 2011, Panahi et al., 2013, Saif et al., 2016].

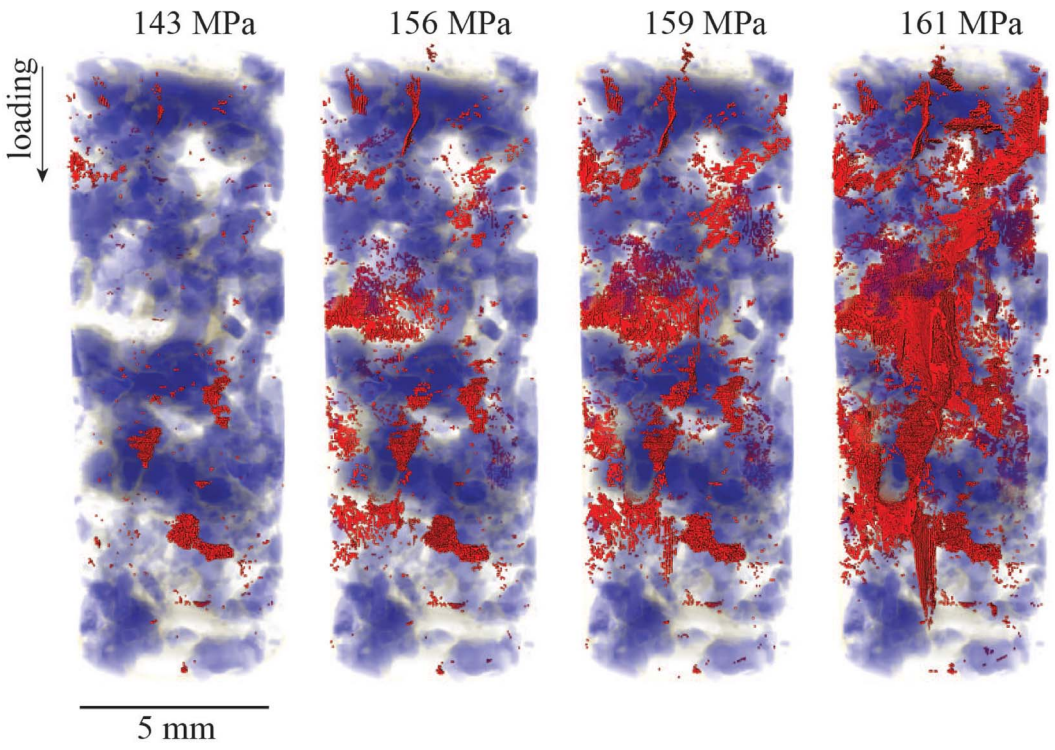

Figure 8. Evolution of a monzonite crystalline rock toward system-size failure under triaxial loading. The rock is represented in blue and grey shades and microfractures that developed during loading are in red. The sample, 5 mm diameter and 10 mm height, was under a constant confining pressure of 25 MPa and the axial loading, indicated above each image, was increased by steps until the sample failed, producing a laboratory earthquake. The final failure was preceded by the nucleation, growth, and coalescence of microfractures in the sample that represent precursors to the final catastrophic failure. See Renard et al. [2019b] for more information about the experiment.

5. Perspectives

Four dimensional XMT imaging has proved its relevance to unravel the complex evolution of minerals and porous and fractured rocks inherent to thermal, chemical, hydrodynamical or mechanical solicitations. The technique provides new insights in the THMC coupled processes occurring in the sub-surface.

The recent upgrade to fourth generation synchrotron facilities, such as the Extreme Brilliant Source at the European Synchrotron Radiation Facility (France) [Rack, 2020], and the coming upgrades at the Advanced Light Source (USA), Spring-8 (Japan), and Swiss Light Source—to cite only the first ones—offers unprecedented opportunities to develop rock physics and flow dynamics experiments. X-ray sources ten to hundred times brighter and with a higher fraction of coherent photons than the third generation of synchrotrons open ways to real-time acquisition in the domain of Digital Rock Physics. Together with the construction of rotation stages that can carry loads of several hundreds kilograms [Cotte et al., 2019] and designed flow-through and triaxial cells for *in situ* imaging, these technology developments contribute to run experiments with unprecedented sample volumes (several cm^3), pressures (up to 1 GPa) and temperature conditions (up to 500 °C), and to characterize processes that progress very quickly. Time limitation for multi-scan imaging or imaging of highly absorbent samples should be overcome, and it will be possible to

perform 3D XMT scans at different sample distances or of dense materials within seconds. A remaining limitation may be how fast the sample can be rotated without interfering with the geological process studied, e.g. through the increase of centrifugal forces that could affect the fluid phase distribution.

Coupling 4D XMT imaging of geological processes with other imaging or monitoring techniques based on X-ray diffraction, X-ray fluorescence, X-ray grating interferometry, or acoustic emission tomography, becomes also possible, providing supplementary data about chemical composition, micro-porosity distribution, mineral phase distribution, characterization of phase transformation, and seismic processes. The increase in brightness and coherence also offers a major step towards multi-scale imaging of samples and processes.

Visualisation of the distribution of the fluid and solid phases in rocks, as evolution of the pore space, rock matrix and interfaces during thermal, flow, mechanical or geochemical reactions will offer in return unprecedented constraints for numerical modelling in multi-phase flow, geomechanics, geophysics or reactive transport domains, in order to unravel the processes at the core during thermo-hydro-mechanico-chemical solicitations of rocks.

For the first time, it is now possible, through both synchrotron technology developments and building of the next generation of core holders and rock deformation apparatuses, to image geological processes as they occur at depth. These developments will open a new era in several domains of geosciences where the study of rock evolution is necessary for progress on important societal challenges in the domains of geo-resources (geothermal energy, storage of energy and wastes), geohazards (earthquakes, landslides, volcanoes and glacier instabilities), and groundwater production.

Conflicts of interest

Authors have no conflict of interest to declare.

Acknowledgments

CN is very grateful to the Académie des Sciences for awarding of the Prize Michel Gouilloud-Schlumberger, and also thanks the Paul Scherrer Insitute for provision of synchrotron radiation beamtime at Swiss Light Source, TOMCAT beamline X02DA. FR acknowledges funding from the European Research Council (ERC) under the European Union's Horizon 2020 research and innovation program (grant agreement No. 101019628 BREAK), the European Synchrotron Radiation Facility for provision of synchrotron radiation facilities, and Benoît Cordonnier for assistance in using beamline ID19.

References

Al-Khulaifi, Y., Lin, Q., Blunt, M. J., and Bijeljic, B. (2017). Reaction rates in chemically heterogeneous rock: Coupled impact of structure and flow properties studied by X-ray microtomography. *Environ. Sci. Technol.*, 51(7), 4108–4116.

Al-Khulaifi, Y., Lin, Q., Blunt, M. J., and Bijeljic, B. (2018). Reservoir-condition pore-scale imaging of dolomite reaction with supercritical CO_2 acidified brine: Effect of pore-structure on reaction rate using velocity distribution analysis. *Int. J. Greenh. Gas Control*, 68, 99–111.

Al-Khulaifi, Y., Lin, Q. Y., Blunt, M. J., and Bijeljic, B. (2019). Pore-scale dissolution by CO_2 saturated brine in a multimineral carbonate at reservoir conditions: Impact of physical and chemical heterogeneity. *Water Resour. Res.*, 55(4), 3171–3193.

Alhosani, A., Bijeljic, B., and Blunt, M. J. (2021). Pore-scale imaging and analysis of wettability order, trapping and displacement in three-phase flow in porous media with various wettabilities. *Transp. Porous Med.*, 140(1), 59–84.

Alhosani, A., Scanziani, A., Lin, Q., Pan, Z., Bijeljic, B., and Blunt, M. J. (2019). In situ pore-scale analysis of oil recovery during three-phase near-miscible CO_2 injection in a water-wet carbonate rock. *Adv. Water Resour.*, 134, article no. 103432.

Alhosani, A., Scanziani, A., Lin, Q., Selem, A., Pan, Z., Blunt, M. J., and Bijeljic, B. (2020). Three-phase flow displacement dynamics and haines jumps in a hydrophobic porous medium. *Proc. R. Soc. A*, 476(2244), article no. 20200671.

Andrew, M., Bijeljic, B., and Blunt, M. J. (2014a). Pore-by-pore capillary pressure measurements using X-ray microtomography at reservoir conditions: Curvature, snap-off, and remobilization of residual CO_2. *Water Resour. Res.*, 50(11), 8760–8774.

Andrew, M., Bijeljic, B., and Blunt, M. J. (2014b). Pore-scale contact angle measurements at reservoir conditions using X-ray microtomography. *Adv. Water Resour.*, 68, 24–31.

Andrews, E., Muggeridge, A., Garfi, G., Jones, A., and Krevor, S. (2021). Pore-scale X-ray imaging of wetting alteration and oil redistribution during low-salinity flooding of berea sandstone. *Energy Fuels*, 35(2), 1197–1207.

Arganda-Carreras, I., Kaynig, V., Rueden, C., Eliceiri, K. W., Schindelin, J., Cardona, A., and Seung, H. S. (2017). Trainable Weka segmentation: a machine learning tool for microscopy pixel classification. *Bioinformatics*, 33(15), 2424–2426.

Bartels, W. B., Racker, M., Boone, M., Bultreys, T., Mahani, H., Berg, S., Hassanizadeh, S. M., and Cnudde, V. (2019). Imaging spontaneous imbibition in full Darcy-scale samples at pore-scale resolution by fast X-ray tomography. *Water Resour. Res.*, 55(8), 7072–7085.

Baruchel, J., Boller, E., Cloetens, P., Ludwig, W., and Peyrin, F. (2000). Microtomography at a third generation synchrotron radiation facility. In Baruchel, J., Buffiere, J., Maire, E., Merle, P., and Peix, G., editors, *X-Ray Tomography in Material Science*, pages 45–59. Hermes Science Publ, Paris.

Bay, B. K., Smith, T. S., Fyhrie, D. P., and Saad, M. (1999). Digital volume correlation: three-dimensional strain mapping using X-ray tomography. *Exp. Mech.*, 39(3), 217–226.

Bear, J. (1972). *Dynamics of Fluids in Porous Media*. Elsevier, Amsterdam.

Bedford, J., Fusseis, F., Leclere, H., Wheeler, J., and Faulkner, D. (2017). A 4D view on the evolution of metamorphic dehydration reactions. *Sci. Rep.*, 7, article no. 6881.

Berg, S., Ott, H., Klapp, S. A., Schwing, A., Neiteler, R., Brussee, N., Makurat, A., Leu, L., Enzmann, F., Schwarz, J.-O., Kersten, M., Irvine, S., and Stampanoni, M. (2013). Real-time 3D imaging of Haines jumps in porous media flow. *Proc. Natl. Acad. Sci. USA*, 110(10), 3755–3759.

Bernard, D., Nielsen, O., Salvo, L., and Cloetens, P. (2005). Permeability assessment by 3D interdendritic flow simulations on microtomography mappings of Al-Cu alloys. *Mater. Sci. Eng. A*, 392(1), 112–120.

Blunt, M. J., Bijeljic, B., Dong, H., Gharbi, O., Iglauer, S., Mostaghimi, P., Paluszny, A., and Pentland, C. (2013). Pore-scale imaging and modelling. *Adv. Water Resour.*, 51, 197–216.

Boon, M., Bijeljic, B., and Krevor, S. (2017). Observations of the impact of rock heterogeneity on solute spreading and mixing. *Water Resour. Res.*, 53(6), 4624–4642.

Boon, M., Bijeljic, B., Niu, B., and Krevor, S. (2016). Observations of 3D transverse dispersion and dilution in natural consolidated rock by X-ray tomography. *Adv. Water Resour.*, 96, 266–281.

Boone, M., De Kock, T., Bultreys, T., De Schutter, G., Vontobel, P., Van Hoorebeke, L., and Cnudde, V. (2014). 3D mapping of water in oolithic limestone at atmospheric and vacuum saturation using X-ray micro-CT differential imaging. *Mater. Charact.*, 97, 150–160.

Bossa, N., Chaurand, P., Vicente, J., Borschneck, D., Levard, C., Aguerre-Chariol, O., and Rose, J. (2015). Micro- and nano-X-ray computed-tomography: A step forward in the characterization of the pore network of a leached cement paste. *Cem. Concr. Res.*, 67, 138–147.

Boulard, E., King, A., Deslandes, J.-P., Le Godec, Y., Perrillat, J.-P., Clark, A., Morard, G., and Itié, J.-P. (2018). High-speed tomography under extreme conditions at the PSICHE beamline of the SOLEIL synchrotron. *J. Synchrotron Radiat.*, 25(3), 818–825.

Brusseau, M. L., Janousek, H., Murao, A., and Schnaar, G. (2008). Synchrotron X-ray microtomography and interfacial partitioning tracer test measurements of NAPL-water interfacial areas. *Water Resour. Res.*, 44(1), article no. W01411.

Buades, A., Coll, B., and Morel, J. (2005). A non-local algorithm for image denoising. In Schmid, C., Soatto, S., and Tomasi, C., editors, *IEEE Conference on Computer Vision and Pattern Recognition*, pages 60–65. IEEE, Piscataway, NJ.

Bultreys, T., De Boever, W., and Cnudde, V. (2016). Imaging and image-based fluid transport modeling at the pore scale in geological materials: A practical introduction to the current state-of-the-art. *Earth Sci. Rev.*, 155, 93–128.

Burlion, N., Bernard, D., and Chen, D. (2006). X-ray microtomography: Application to microstructure analysis of a cementitious material during leaching process. *Cem. Concr. Res.*, 36(2), 346–357.

Butler, I., Fusseis, F., Cartwright-Taylor, A., and Flynn, M. (2020). Mjölnir: a miniature triaxial rock defor-

mation apparatus for 4D synchrotron X-ray microtomography. *J. Synchrotron Radiat.*, 27(6), 1681–1687.

Carlson, W. D. (2006). Three-dimensional imaging of earth and planetary materials. *Earth Planet. Sci. Lett.*, 249(3), 133–147.

Carlson, W. D., Rowe, T., Ketcham, R. A., and Colbert, M. W. (2003). Applications of high-resolution X-ray computed tomography in petrology, meteoritics and palaeontology. In Mees, F., Swennen, R., Van Geet, M., and Jacobs, P., editors, *Applications of X-Ray Computed Tomography in the Geosciences*, volume 215 of *Special Publication*, pages 7–22. Geological Society, London.

Cartwright-Taylor, A., Main, I. G., Butler, I. B., Fusseis, F., Flynn, M., and King, A. (2020). Catastrophic failure: How and when? insights from 4-D in situ X-ray microtomography. *J. Geophys. Res. Solid Earth*, 125(8), article no. e2020JB019642.

Chen, M.-R., Hinkley, R. E., and Killough, J. E. (1996). Computed tomography imaging of air sparging in porous media. *Water Resour. Res.*, 32(10), 3013–3024.

Cil, M., Schabelski, J., Packman, A., and Buscarnera, G. (2019). A miniaturized testing apparatus to study the chemo-mechanics of porous media. *Geotech. Test. J.*, 43(4), 829–843.

Cloetens, P., Barrett, R., Baruchel, J., Guigay, J.-P., and Schlenker, M. (1996). Phase objects in synchrotron radiation hard X-ray imaging. *J. Phys. D: Appl. Phys.*, 29(1), 133–146.

Cnudde, V. and Boone, M. N. (2013). High-resolution X-ray computed tomography in geosciences: A review of the current technology and applications. *Earth Sci. Rev.*, 123, 1–17.

Coles, M. E., Hazlett, R. D., Muegge, E. L., Jones, K. W., Andrews, B., Dowd, B., Siddons, P., and Peskin, A. (1998). Developments in synchrotron X-ray microtomography with applications to flow in porous media. *SPE Reserv. Evaluation Eng.*, 1(4), 288–296.

Cotte, M., Autran, P.-O., Berruyer, C., Dejoie, C., Susini, J., and Tafforeau, P. (2019). Cultural and natural heritage at the ESRF: Looking back and to the future. *Synchrotron Radiat. News*, 32(6), 34–40.

Culligan, K. A., Wildenschild, D., Christensen, B. S. B., Gray, W. G., Rivers, M. L., and Tompson, A. F. B. (2004). Interfacial area measurements for unsaturated flow through a porous medium. *Water Resour. Res.*, 40(12), article no. W12413.

Darcy, H. (1856). *Les Fontaines Publiques De La Ville De Dijon*. Victor Dalmont, Paris.

De Kock, T., Boone, M. A., De Schryver, T., Van Stappen, J., Derluyn, H., Masschaele, B., De Schutter, G., and Cnudde, V. (2015). A pore-scale study of fracture dynamics in rock using X-ray micro-CT under ambient freeze–thaw cycling. *Environ. Sci. Technol.*, 49(5), 2867–2874.

DeCarlo, K. F. and Shokri, N. (2014). Salinity effects on cracking morphology and dynamics in 3D desiccating clays. *Water Resour. Res.*, 50(4), 3052–3072.

Dewanckele, J., De Kock, T., Boone, M. A., Cnudde, V., Brabant, L., Boone, M. N., Fronteau, G., Van Hoorebeke, L., and Jacobs, P. (2012). 4d imaging and quantification of pore structure modifications inside natural building stones by means of high resolution X-ray CT. *Sci. Total Environ.*, 416, 436–448.

Dubsky, S., Jamison, R. A., Higgins, S. P. A., Siu, K. K. W., Hourigan, K., and Fouras, A. (2012). Computed tomographic X-ray velocimetry for simultaneous 3D measurement of velocity and geometry in opaque vessels. *Exp. Fluids*, 52(3), 543–554.

Duchon, C. E. (1979). Lanczos filtering in one and two dimensions. *J. Appl. Meteorol. Climatol.*, 18(8), 1016–1022.

Eckley, S. A. and Ketcham, R. A. (2019). 4D imaging of mineral dissolution in porous carbonado diamond: Implications for acid digestion and XCT measurement of porosity and material properties. *Front. Earth Sci.*, 7, article no. 288.

Ellis, B. R., Fitts, J. P., Bromhal, G. S., McIntyre, D. L., Tappero, R., and Peters, C. A. (2013). Dissolution-driven permeability reduction of a fractured carbonate caprock. *Environ. Eng. Sci.*, 30(4), 187–193.

Fusseis, F., Schrank, C., Liu, J., Karrech, A., Llana-Funez, S., Xiao, X., and Regenauer-Lieb, K. (2012). Pore formation during dehydration of a polycrystalline gypsum sample observed and quantified in a time-series synchrotron X-ray microtomography experiment. *Solid Earth*, 3(1), 71–86.

Fusseis, F., Steeb, H., Xiao, X., Zhu, W.-l., Butler, I. B., Elphick, S., and Mäder, U. (2014a). A low-cost X-ray-transparent experimental cell for synchrotron-based X-ray microtomography studies under geological reservoir conditions. *J. Synchrotron Radiat.*, 21(1), 251–253.

Fusseis, F., Xiao, X., Schrank, C., and De Carlo, F.

(2014b). A brief guide to synchrotron radiation-based microtomography in (structural) geology and rock mechanics. *J. Struct. Geol.*, 65, 1–16.

Gao, X., Yang, Y., Yang, S., Ma, Y., and Chen, M. (2021). Microstructure evolution of chalcopyrite agglomerates during leaching a synchrotron-based X-ray CT approach combined with a data-constrained modelling (DCM). *Hydrometallurgy*, 201, article no. 105586.

García-Moreno, F., Kamm, P. H., Neu, T. R., Bülk, F., Mokso, R., Schlepütz, C. M., Stampanoni, M., and Banhart, J. (2019). Using X-ray tomoscopy to explore the dynamics of foaming metal. *Nat. Commun.*, 10(1), article no. 3762.

Garcia-Rio, M., Cama, J., Luquot, L., and Soler, J. M. (2014). Interaction between CO_2-rich sulfate solutions and carbonate reservoir rocks from atmospheric to supercritical CO_2 conditions: Experiments and modeling. *Chem. Geol.*, 383, 107–122.

Giovenco, E., Perrillat, J.-P., Boulard, E., King, A., Guignot, N., and Le Godec, Y. (2021). Quantitative 4D X-ray microtomography under extreme conditions: a case study on magma migration. *J. Synchrotron Radiat.*, 28, 1598–1609.

Godinho, J. R. A., Gerke, K. M., Stack, A. G., and Lee, P. D. (2016). The dynamic nature of crystal growth in pores. *Sci. Rep.*, 6, article no. 33086.

Godinho, J. R. A. and Withers, P. J. (2018). Time-lapse 3D imaging of calcite precipitation in a microporous column. *Geochim. Cosmochim. Acta*, 222, 156–170.

Golfier, F., Zarcone, C., Bazin, B., Lenormand, R., Lasseux, D., and Quintard, M. (2002). On the ability of a Darcy-scale model to capture wormhole formation during the dissolution of a porous medium. *J. Fluid Mech.*, 457, 213–254.

Gouze, P., Edlmann, K., McDermott, C. I., and Luquot, L. (2017). *Laboratory Experiments*. Springer, Cham.

Gouze, P., Noiriel, C., Bruderer, C., Loggia, D., and Leprovost, R. (2003). X-ray tomography characterisation of fracture surfaces during dissolution. *Geophys. Res. Lett.*, 30(5), article no. 1267.

Gratier, J. P., Noiriel, C., and Renard, F. (2015). Experimental evidence of rock layering development by pressure solution. *Geology*, 43(10), 871–874.

Guignot, N., King, A., and Boulard, E. (2020). Synchrotron X-ray computed microtomography for high pressure science. *J. Appl. Phys.*, 127(24), article no. 240901.

Hall, S. A., Bornert, M., Desrues, J., Pannier, Y., Lenoir, N., Viggiani, G., and Bésuelle, P. (2010). Discrete and continuum analysis of localised deformation in sand using X-ray μCT and volumetric digital image correlation. *Géotechnique*, 60(5), 315–322.

Hasan, A. and Alshibli, K. (2012). Three dimensional fabric evolution of sheared sand. *Granul. Matter*, 14(4), 469–482.

Heap, M. J., Baud, P., McBeck, J. A., Renard, F., Carbillet, L., and Hall, S. A. (2020). Imaging strain localisation in porous andesite using digital volume correlation. *J. Volcanol. Geotherm. Res.*, 404, article no. 107038.

Hébert, V., Garing, C., Luquot, L., Pezard, P. A., and Gouze, P. (2015). Multi-scale X-ray tomography analysis of carbonate porosity. In Agar, S. M. and Geiger, S., editors, *Fundamental Controls on Fluid Flow in Carbonates: Current Workflows to Emerging Technologies*, volume 409, pages 61–79. Geological Society, London.

Herring, A. L., Andersson, L., Newell, D. L., Carey, J. W., and Wildenschild, D. (2014). Pore-scale observations of supercritical CO_2 drainage in bentheimer sandstone by synchrotron X-ray imaging. *Int. J. Greenh. Gas Control*, 25, 93–101.

Huang, L., Baud, P., Cordonnier, B., Renard, F., Liu, L., and Wong, T.-f. (2019). Synchrotron X-ray imaging in 4d: multiscale failure and compaction localization in triaxially compressed porous limestone. *Earth Planet. Sci. Lett.*, 528, article no. 115831.

Iglauer, S. and Lebedev, M. (2018). High pressure-elevated temperature X-ray micro-computed tomography for subsurface applications. *Adv. Colloid Interface Sci.*, 256, 393–410.

Iglauer, S., Paluszny, A., Pentland, C. H., and Blunt, M. J. (2011). Residual CO_2 imaged with X-ray micro-tomography. *Geophys. Res. Lett.*, 38, article no. L21403.

Javanbakht, G., Arshadi, M., Qin, T., and Goual, L. (2017). Micro-scale displacement of napl by surfactant and microemulsion in heterogeneous porous media. *Adv. Water Resour.*, 105, 173–187.

Karpyn, Z. T., Grader, A. S., and Halleck, P. M. (2007). Visualization of fluid occupancy in a rough fracture using micro-tomography. *J. Colloid Interface Sci.*, 307(1), 181–187.

Keyes, S. D., Cooper, L., Duncan, S., Koebernick, N., McKay Fletcher, D. M., Scotson, C. P., van Veelen, A., Sinclair, I., and Roose, T. (2017). Measure-

ment of micro-scale soil deformation around roots using four-dimensional synchrotron tomography and image correlation. *J. R. Soc. Interface*, 14(136), article no. 20170560.

Keyes, S. D., Gillard, F., Soper, N., Mavrogordato, M. N., Sinclair, I., and Roose, T. (2016). Mapping soil deformation around plant roots using in vivo 4d X-ray computed tomography and digital volume correlation. *J. Biomech.*, 49(9), 1802–1811.

Kim, M., Kim, K.-Y., Lim, J.-H., Kim, C. Y., Kim, S.-G., Han, G., Han, W. S., and Park, E. (2022). Pore-scale investigation of dynamic immiscible displacement in layered media using synchrotron X-ray microtomography. *Environ. Sci. Technol.*, 56(1), 282–292.

Kim, W., Kanezaki, A., and Tanaka, M. (2020). Unsupervised learning of image segmentation based on differentiable feature clustering. *IEEE Trans. Image Process.*, 29, 8055–8068.

Kim, Y., Abdilla, B., Yuan, K., De Andrade, V., Sturchio, N. C., Lee, S. S., and Fenter, P. (2021). Replacement of calcium carbonate polymorphs by cerussite. *ACS Earth and Space Chem.*, 5(9), 2433–2441.

Kobchenko, M., Panahi, H., Renard, F., Dysthe, D. K., Malthe-Sørenssen, A., Mazzini, A., Scheibert, J., Jamtveit, B., and Meakin, P. (2011). 4D imaging of fracturing in organic-rich shales during heating. *J. Geophys. Res. Solid Earth*, 116(B12), article no. B12201.

Kodali, P., Dhawan, N., Depci, T., Lin, C. L., and Miller, J. D. (2011). Particle damage and exposure analysis in HPGR crushing of selected copper ores for column leaching. *Miner. Eng.*, 24(13), 1478–1487.

Kurganskaya, I. and Luttge, A. (2016). Kinetic Monte Carlo approach to study carbonate dissolution. *J. Phys. Chem. C*, 120(12), 6482–6492.

Leger, M., Roubinet, D., Jamet, M., and Luquot, L. (2022). Impact of hydro-chemical conditions on structural and hydro-mechanical properties of chalk samples during dissolution experiments. *Chem. Geol.*, 594, article no. 120763.

Lenoir, N., Bornert, M., Desrues, J., Bésuelle, P., and Viggiani, G. (2007). Volumetric digital image correlation applied to X-ray microtomography images from triaxial compression tests on argillaceous rock. *Strain*, 43(3), 193–205.

Li, X., Akbarabadi, M., Karpyn, Z. T., Piri, M., and Bazilevskaya, E. (2015). Experimental investigation of carbon dioxide trapping due to capillary retention in saline aquifers. *Geofluids*, 15(4), 563–576.

Lin, Q., Bijeljic, B., Pini, R., Blunt, M. J., and Krevor, S. (2018). Imaging and measurement of pore-scale interfacial curvature to determine capillary pressure simultaneously with relative permeability. *Water Resour. Res.*, 54(9), 7046–7060.

Lo, A., Nosrati, A., and Addai-Mensah, J. (2016). Particle and pore dynamics under column leaching of goethitic and saprolitic nickel laterite agglomerates. *Adv. Powder Technol.*, 27(6), 2370–2376.

Louis, L., Wong, T.-F., and Baud, P. (2007). Imaging strain localization by X-ray radiography and digital image correlation: Deformation bands in Rothbach sandstone. *J. Struct. Geol.*, 29(1), 129–140.

Luquot, L., Abdoulghafour, H., and Gouze, P. (2013). Hydro-dynamically controlled alteration of fractured portland cements flowed by CO_2-rich brine. *Int. J. Greenh. Gas Control*, 16, 167–179.

Luquot, L. and Gouze, P. (2009). Experimental determination of porosity and permeability changes induced by injection of CO_2 into carbonate rocks. *Chem. Geol.*, 265(12), 148–159.

Luquot, L., Rodriguez, O., and Gouze, P. (2014). Experimental characterization of porosity structure and transport property changes in limestone undergoing different dissolution regimes. *Transp. Porous Med.*, 101(3), 507–532.

Macente, A., Vanorio, T., Miller, K. J., Fusseis, F., and Butler, I. B. (2019). Dynamic evolution of permeability in response to chemo-mechanical compaction. *J. Geophys. Res. Solid Earth*, 124(11), 11204–11217.

Maes, F., Collignon, A., Vandermeulen, D., Marchal, G., and Suetens, P. (1997). Multimodality image registration by maximization of mutual information. *IEEE Trans. Med. Imaging*, 16(2), 187–198.

Maire, E., Buffiere, J.-Y., Salvo, L., Blandin, J. J., Ludwig, W., and Letang, J. M. (2001). On the application of X-ray microtomography in the field of materials science. *Adv. Eng. Mater.*, 3(8), 539–546.

Maire, E. and Withers, P. J. (2014). Quantitative X-ray tomography. *Int. Mater. Rev.*, 59(1), 1–43.

Mäkiharju, S. A., Dewanckele, J., Boone, M., Wagner, C., and Griesser, A. (2021). Tomographic X-ray particle tracking velocimetry. *Exp. Fluids*, 63(1), article no. 16.

Marone, F., Muench, B., and Stampanoni, M. (2010). Fast reconstruction algorithm dealing with tomog-

raphy artifacts. In Stock, S., editor, *Developments in X-Ray Tomography VII*, volume 7804 of *SPIE, Proceedings of SPIE*, pages 292–302. Conference on Developments in X-Ray Tomography VII, San Diego, CA, 2010.

Marone, F., Schlepütz, C. M., Marti, S., Fusseis, F., Velásquez-Parra, A., Griffa, M., Jiménez-Martínez, J., Dobson, K. J., and Stampanoni, M. (2020). Time resolved in situ X-ray tomographic microscopy unraveling dynamic processes in geologic systems. *Front. Earth Sci.*, 7, article no. 346.

Marone, F., Studer, A., Billich, H., Sala, L., and Stampanoni, M. (2017). Towards on-the-fly data post-processing for real-time tomographic imaging at TOMCAT. *Adv. Struct. Chem. Imaging*, 3(1), article no. 1.

Marti, S., Fusseis, F., Butler, I. B., Schlepuetz, C., Marone, F., Gilgannon, J., Kilian, R., and Yang, Y. (2021). Time-resolved grain-scale 3D imaging of hydrofracturing in halite layers induced by gypsum dehydration and pore fluid pressure buildup. *Earth Planet. Sci. Lett.*, 554, article no. 116679.

McBeck, J., Aiken, J. M., Ben-Zion, Y., and Renard, F. (2020). Predicting the proximity to macroscopic failure using local strain populations from dynamic in situ X-ray tomography triaxial compression experiments on rocks. *Earth Planet. Sci. Lett.*, 543, article no. 116344.

McBeck, J., Kobchenko, M., Hall, S. A., Tudisco, E., Cordonnier, B., Meakin, P., and Renard, F. (2018). Investigating the onset of strain localization within anisotropic shale using digital volume correlation of time-resolved X-ray microtomography images. *J. Geophys. Res. Solid Earth*, 123(9), 7509–7528.

McDonald, S., Marone, F., Hintermuller, C., Mikuljan, G., David, C., Pfeiffer, F., and Stampanoni, M. (2009). Advanced phase-contrast imaging using a grating interferometer. *J. Synchrotron Radiat.*, 16, 562–572.

Menefee, A. H., Welch, N. J., Frash, L. P., Hicks, W., Carey, J. W., and Ellis, B. R. (2020). Rapid mineral precipitation during shear fracturing of carbonate-rich shales. *J. Geophys. Res. Solid Earth*, 125(6), article no. e2019JB018864.

Menke, H. P., Andrew, M. G., Blunt, M. J., and Bijeljic, B. (2017a). Reservoir condition imaging of reactive transport in heterogeneous carbonates using fast synchrotron tomography : Effect of initial pore structure and flow conditions. *Chem. Geol.*, 428, 15–26.

Menke, H. P., Bijeljic, B., Andrew, M. G., and Blunt, M. J. (2015). Dynamic three-dimensional pore-scale imaging of reaction in a carbonate at reservoir conditions. *Environ. Sci. Technol.*, 49(7), 4407–4414.

Menke, H. P., Bijeljic, B., and Blunt, M. J. (2017b). Dynamic reservoir-condition microtomography of reactive transport in complex carbonates: Effect of initial pore structure and initial brine pH. *Geochim. Cosmochim. Acta*, 204, 267–285.

Menke, H. P., Reynolds, C. A., Andrew, M. G., Nunes, J. P. P., Bijeljic, B., and Blunt, M. J. (2018). 4D multi-scale imaging of reactive flow in carbonates: Assessing the impact of heterogeneity on dissolution regimes using streamlines at multiple length scales. *Chem. Geol.*, 481, 27–37.

Meyer, F. and Beucher, S. (1990). Morphological segmentation. *J. Vis. Commun. Image Represent.*, 1(1), 21–46.

Molnar, I. L., Gerhard, J. I., Willson, C. S., and O'Carroll, D. M. (2015). The impact of immobile zones on the transport and retention of nanoparticles in porous media. *Water Resour. Res.*, 51(11), 8973–8994.

Molnar, I. L., Sanematsu, P. C., Gerhard, J. I., Willson, C. S., and O'Carroll, D. M. (2016). Quantified pore-scale nanoparticle transport in porous media and the implications for colloid filtration theory. *Langmuir*, 32(31), 7841–7853.

Noiriel, C. (2015). Resolving time-dependent evolution of pore scale structure, permeability and reactivity using X-ray microtomography. In Steefel, C. I., Emmanuel, E., and Anovitz, L., editors, *Pore Scale Geochemical Processes*, volume 80 of *Reviews in Mineralogy & Geochemistry*, pages 247–286. Mineralogical Society of America, Chantilly, VA.

Noiriel, C., Bernard, D., Gouze, P., and Thibaut, X. (2005). Hydraulic properties and microgeometry evolution in the course of limestone dissolution by CO_2-enriched water. *Oil Gas Sci. Technol.*, 60(1), 177–192.

Noiriel, C., Gouze, P., and Bernard, D. (2004). Investigation of porosity and permeability effects from microstructure changes during limestone dissolution. *Geophys. Res. Lett.*, 31(24), article no. L24603.

Noiriel, C., Gouze, P., and Madé, B. (2007a). Time-

resolved 3D characterisation of flow and dissolution patterns in a single rough-walled fracture. In Krasny, J. and Sharp, J., editors, *IAH Selected Papers Series 9 on Groundwater in Fractured Rocks*, pages 629–642. Taylor & Francis, Oxfordshire.

Noiriel, C., Gouze, P., and Made, B. (2013). 3D analysis of geometry and flow changes in a limestone fracture during dissolution. *J. Hydrol.*, 486, 211–223.

Noiriel, C., Madé, B., and Gouze, P. (2007b). Impact of coating development on the hydraulic and transport properties in argillaceous limestone fracture. *Water Resour. Res.*, 43, article no. W09046.

Noiriel, C., Oursin, M., and Daval, D. (2020). Examination of crystals in 3D using X-ray microtomography: a way to reconciliate rates at the laboratory? *Geochem. Cosmochim. Acta*, 273, 1–25.

Noiriel, C., Oursin, M., Saldi, G. D., and Haberthür, D. (2019). Direct determination of dissolution rates at crystal surface using 3D X-ray micro-tomography. *Earth Space Chem.*, 3(1), 101–108.

Noiriel, C., Seigneur, N., Guern, P. L., and Lagneau, V. (2021). Geometry and mineral heterogeneity controls on precipitation in fractures: An X-ray micro-tomography and reactive transport modeling study. *Adv. Water Resour.*, 152, article no. 103916.

Noiriel, C. and Soulaine, C. (2021). Pore-scale imaging and modelling of reactive flow in evolving porous media: Tracking the dynamics of the fluidrock interface. *Transp. Porous Med.*, 140(1), 181–213.

Noiriel, C., Steefel, C. I., Yang, L., and Ajo-Franklin, J. (2012). Upscaling calcium carbonate precipitation rates from pore to continuum scale. *Chem. Geol.*, 318–319, 60–74.

Noiriel, C., Steefel, C. I., Yang, L., and Bernard, D. (2016). Effects of pore-scale heterogeneous precipitation on permeability and flow. *Adv. Water Resour.*, 95, 125–137.

Oren, P. E., Ruspini, L. C., Saadatfar, M., Sok, R. M., Knackstedt, M., and Herring, A. (2019). In-situ pore-scale imaging and image-based modelling of capillary trapping for geological storage of CO_2. *Int. J. Greenh. Gas Control*, 87, 34–43.

Pak, T., Archilha, N. L., Mantovani, I. F., Moreira, A. C., and Butler, I. B. (2018). The dynamics of nanoparticle-enhanced fluid displacement in porous media - a pore-scale study. *Sci. Rep.*, 8, 11148.

Pak, T., Luz, L. F. D. L., Tosco, T., Costa, G. S. R., Rosa, P. R. R., and Archilha, N. L. (2020). Pore-scale investigation of the use of reactive nanoparticles for in situ remediation of contaminated groundwater source. *Proc. Natl. Acad. Sci. USA*, 117(24), 13366–13373.

Panahi, H., Meakin, P., Renard, F., Kobchenko, M., Scheibert, J., Mazzini, A., Jamtveit, B., Malthe-Sorenssen, A., and Dysthe, D. K. (2013). A 4D synchrotron X-ray-tomography study of the formation of hydrocarbon-migration pathways in heated organic-rich shale. *SPE J.*, 18(02), 366–377.

Peng, S., Marone, F., and Dultz, S. (2014). Resolution effect in X-ray microcomputed tomography imaging and small pore's contribution to permeability for a berea sandstone. *J. Hydrol.*, 510, 403–411.

Philippe, J., Le Godec, Y., Mezouar, M., Berg, M., Bromiley, G., Bergame, F., Perrillat, J. P., Alvarez-Murga, M., Morand, M., Atwood, R., King, A., and Régnier, S. (2016). Rotating tomography Paris–Edinburgh cell: a novel portable press for micro-tomographic 4D imaging at extreme pressure/temperature/stress conditions. *High Press. Res.*, 36(4), 512–532.

Polak, A., Grader, A. S., Wallach, R., and Nativ, R. (2003). Chemical diffusion between a fracture and the surrounding matrix: Measurement by computed tomography and modeling. *Water Resour. Res.*, 39(4), 10–1–10–13.

Porter, M. L., Wildenschild, D., Grant, G., and Gerhard, J. I. (2010). Measurement and prediction of the relationship between capillary pressure, saturation, and interfacial area in a NAPL-water-glass bead system. *Water Resour. Res.*, 46, article no. W08512.

Privalov, V., Randi, A., Sterpenich, J., Pironon, J., and Morlot, C. (2019). Structural control of a dissolution network in a limestone reservoir forced by radial injection of CO_2 saturated solution: Experimental results coupled with X-ray computed tomography. *Geosciences*, 9(1), article no. 33.

Qajar, J. and Arns, C. H. (2017a). Characterization of reactive flow-induced evolution of carbonate rocks using digital core analysis - part 1: Assessment of pore-scale mineral dissolution and deposition. *J. Contam. Hydrol.*, 192, 60–86.

Qajar, J. and Arns, C. H. (2017b). Characterization of reactive flow-induced evolution of carbonate rocks using digital core analysis - part 2: Calculation of

the evolution of percolation and transport properties. *J. Contam. Hydrol.*, 204, 11–27.

Qajar, J. and Arns, C. H. (2022). Chemically induced evolution of morphological and connectivity characteristics of pore space of complex carbonate rock via digital core analysis. *Water Resour. Res.*, 58(3), article no. e2021WR031298.

Qin, T., Goual, L., Piri, M., Hu, Z., and Wen, D. (2020). Pore-scale dynamics of nanofluid-enhanced NAPL displacement in carbonate rock. *J. Contam. Hydrol.*, 230, article no. 103598.

Rack, A. (2020). Hard X-ray imaging at ESRF: exploiting contrast and coherence with the new EBS storage ring. *Synchrotron Radiat. News*, 33(3), 20–28.

Rad, M. N., Shokri, N., and Sahimi, M. (2013). Pore-scale dynamics of salt precipitation in drying porous media. *Phys. Rev. E*, 88(3), article no. 032404.

Ram, R., Beiza, L., Becker, M., Pownceby, M. I., Chen, M., Yang, Y., Yang, S., and Petersen, J. (2020). Study of the leaching and pore evolution in large particles of a sulfide ore. *Hydrometallurgy*, 192, article no. 105261.

Randi, A., Sterpenich, J., Morlot, C., Pironon, J., Kervevan, C., Beddelem, M., and Flehoc, C. (2014). CO_2-dissolved: a novel concept coupling geological storage of dissolved CO_2 and geothermal heat recovery. Part 3: Design of the MIRAGES-2 experimental device dedicated to the study of the geochemical water-rock interactions triggered by CO_2 laden brine injection. *Energy Procedia*, 63, 4536–4547.

Rane, K., Zhang, B., and Goual, L. (2021). Microscale investigation of DNAPL displacement by engineered graphene quantum dots in heterogeneous porous media. *Colloids Surf. A*, 625, article no. 126936.

Renard, F. (2012). Microfracturation in rocks: from microtomography images to processes. *Eur. Phys. J. Appl. Phys.*, 60(2), article no. 24203.

Renard, F., Bernard, D., Boller, E., and Thibaut, X. (2004). Synchrotron 3D microtomography of halite aggregates during experimental pressure solution creep and evolution of the permeability. *Geophys. Res. Lett.*, 31, article no. L07607.

Renard, F., Cordonnier, B., Dysthe, D. K., Boller, E., Tafforeau, P., and Rack, A. (2016). A deformation rig for synchrotron microtomography studies of geomaterials under conditions down to 10 km depth in the earth. *J. Synchrotron Radiat.*, 23(4), 1030–1034.

Renard, F., McBeck, J., Cordonnier, B., Zheng, X., Kandula, N., Sanchez, J. R., Kobchenko, M., Noiriel, C., Zhu, W., Meakin, P., Fusseis, F., and Dysthe, D. K. (2019a). Dynamic in situ three-dimensional imaging and digital volume correlation analysis to quantify strain localization and fracture coalescence in sandstone. *Pure Appl. Geophys.*, 176(3), 1083–1115.

Renard, F., McBeck, J., Kandula, N., Cordonnier, B., Meakin, P., and Ben-Zion, Y. (2019b). Volumetric and shear processes in crystalline rock approaching faulting. *Proc. Natl. Acad. Sci. USA*, 116(33), 16234–16239.

Renard, F., Weiss, J., Mathiesen, J., Ben-Zion, Y., Kandula, N., and Cordonnier, B. (2018). Critical evolution of damage toward system-size failure in crystalline rock. *J. Geophys. Res. Solid Earth*, 123(2), 1969–1986.

Reynolds, C. A., Menke, H., Andrew, M., Blunt, M. J., and Krevor, S. (2017). Dynamic fluid connectivity during steady-state multiphase flow in a sandstone. *Proc. Natl. Acad. Sci. USA*, 114(31), 8187–8192.

Rougelot, T., Burlion, N., Bernard, D., and Skoczylas, F. (2009). About microcracking due to leaching in cementitious composites: X-ray microtomography description and numerical approach. *Cem. Concr. Res.*, 40(2), 271–283.

Rucker, M., Georgiadis, A., Armstrong, R. T., Ott, H., Brussee, N., van der Linde, H., Simon, L., Enzmann, F., Kersten, M., and Berg, S. (2021). The origin of non-thermal fluctuations in multiphase flow in porous media. *Front. Water*, 3, article no. 671399.

Saenger, E. H., Lebedev, M., Uribe, D., Osorno, M., Vialle, S., Duda, M., Iglauer, S., and Steeb, H. (2016). Analysis of high-resolution X-ray computed tomography images of Bentheim sandstone under elevated confining pressures. *Geophys. Prospect.*, 64(4), 848–859.

Saif, T., Lin, Q., Singh, K., Bijeljic, B., and Blunt, M. J. (2016). Dynamic imaging of oil shale pyrolysis using synchrotron X-ray microtomography. *Geophys. Res. Lett.*, 43(13), 6799–6807.

Scanziani, A., Singh, K., Blunt, M. J., and Guadagnini, A. (2017). Automatic method for estimation of in situ effective contact angle from X-ray micro tomography images of two-phase flow in porous media. *J. Colloid Interface Sci.*, 496, 51–59.

Scanziani, A., Singh, K., Bultreys, T., Bijeljic, B., and Blunt, M. J. (2018). In situ characterization of immiscible three-phase flow at the pore scale for a water-wet carbonate rock. *Adv. Water Resour.*, 121, 446–455.

Scanziani, A., Singh, K., Menke, H., Bijeljic, B., and Blunt, M. J. (2020). Dynamics of enhanced gas trapping applied to CO_2 storage in the presence of oil using synchrotron X-ray micro-tomography. *Appl. Energy*, 259, article no. 114136.

Seright, R. S., Liang, J., Lindquist, W. B., and Dunsmuir, J. H. (2002). Characterizing disproportionate permeability reduction using synchrotron X-ray computed microtomography. *SPE Reserv. Evaluation Eng.*, 5(5), 355–364.

Sethian, J. (1999). *Level Set Methods and Fast Marching Methods: Evolving Interfaces in Computational Geometry, Fluid Mechanics, Computer Vision and Materials Sciences*. Cambridge University Press, Cambridge, 2nd edition.

She, Y., Zhang, C., Mahardika, M. A., Patmonoaji, A., Hu, Y., Matsushita, S., and Suekane, T. (2021). Pore-scale study of in-situ surfactant flooding with strong oil emulsification in sandstone based on X-ray microtomography. *J. Ind. Eng. Chem.*, 98, 247–261.

Silin, D., Tomutsa, L., Benson, S. M., and Patzek, T. W. (2011). Microtomography and pore-scale modeling of two-phase fluid distribution. *Transp. Porous Med.*, 86(2), 525–545.

Singh, K., Bijeljic, B., and Blunt, M. J. (2016). Imaging of oil layers, curvature and contact angle in a mixed-wet and a water-wet carbonate rock. *Water Resour. Res.*, 52(3), 1716–1728.

Singh, K., Menke, H., Andrew, M., Lin, Q., Rau, C., Blunt, M. J., and Bijeljic, B. (2017). Dynamics of snap-off and pore-filling events during two-phase fluid flow in permeable media. *Sci. Rep.*, 7, article no. 5192.

Sittner, J., Godinho, J. R. A., Renno, A. D., Cnudde, V., Boone, M., De Schryver, T., Van Loo, D., Merkulova, M., Roine, A., and Liipo, J. (2021). Spectral X-ray computed micro-tomography: 3-dimensional chemical imaging. *X-Ray Spectrom.*, 50(2), 92–105.

Smith, M. M., Sholokhova, Y., Hao, Y., and Carroll, S. A. (2013). CO_2-induced dissolution of low permeability carbonates. Part i: Characterization and experiments. *Adv. Water Resour.*, 62, 370–387.

Spanne, P., Thovert, J. F., Jacquin, C. J., Lindquist, W. B., Jones, K. W., and Adler, P. M. (1994). Synchrotron computed microtomography of porous media: topology and transport. *Phys. Rev. Lett.*, 73(14), 2001–2004.

Spokas, K., Fang, Y., Fitts, J. P., Peters, C. A., and Elsworth, D. (2019). Collapse of reacted fracture surface decreases permeability and frictional strength. *J. Geophys. Res. Solid Earth*, 59, article no. e2019WR026112.

Spurin, C., Bultreys, T., Rücker, M., Garfi, G., Schlepütz, C. M., Novak, V., Berg, S., Blunt, M. J., and Krevor, S. (2020). Real-time imaging reveals distinct pore-scale dynamics during transient and equilibrium subsurface multiphase flow. *Water Resour. Res.*, 56(12), article no. e2020WR028287.

Suuronen, J. P. and Sayab, M. (2018). 3d nanopetrography and chemical imaging of datable zircons by synchrotron multimodal X-ray tomography. *Sci. Rep.*, 8(1), article no. 4747.

Tanino, Y. and Blunt, M. J. (2012). Capillary trapping in sandstones and carbonates: Dependence on pore structure. *Water Resour. Res.*, 48, article no. W08525.

Tissot, B., Pelet, R., and Ungerer, P. (1987). Thermal history of sedimentary basins, maturation indices, and kinetics of oil and gas generation. *Am. Assoc. Pet. Geol. Bull.*, 71(12), 1445–1466.

Tudisco, E., Andò, E., Cailletaud, R., and Hall, S. A. (2017). Tomowarp2: A local digital volume correlation code. *SoftwareX*, 6, 267–270.

Turner, M. L. et al. (2004). Three-dimensional imaging of multiphase flow in porous media. *Physica A*, 339(1), 166–172.

Unsal, E., Rucker, M., Berg, S., Bartels, W. B., and Bonnin, A. (2019). Imaging of compositional gradients during in situ emulsification using X-ray microtomography. *J. Colloid Interface Sci.*, 550, 159–169.

Van Geet, M., Swennen, R., and Wevers, M. (2001). Toward 3D petrography: application of microfocus computer tomography in geological science. *Comput. Geosci.*, 27, 1091–1099.

Van Offenwert, S., Cnudde, V., and Bultreys, T. (2019). Pore-scale visualization and quantification of transient solute transport using fast microcomputed tomography. *Water Resour. Res.*, 55(11), 9279–9291.

Van Stappen, J. F. et al. (2018). In situ triaxial testing to determine fracture permeability and aperture distribution for CO_2 sequestration in Svalbard, Norway. *Environ. Sci. Technol.*, 52(8), 4546–4554.

Vialle, S., Contraires, S., Zinzsner, B., Clavaud, J. B., Mahiouz, K., Zuddas, P., and Zamora, M. (2014). Percolation of CO_2-rich fluids in a limestone sample: Evolution of hydraulic, electrical, chemical, and structural properties. *J. Geophys. Res. Solid Earth*, 119(4), 2828–2847.

Viggiani, G., Lenoir, N., Bésuelle, P., Di Michiel, M., Marello, S., Desrues, J., and Kretzschmer, M. (2004). X-ray microtomography for studying localized deformation in fine-grained geomaterials under triaxial compression. *C. R. Mec.*, 332(10), 819–826.

Villanova, J. et al. (2017). Fast in situ 3D nanoimaging: A new tool for dynamic characterization in materials science. *Mater. Today*, 20(7), 354–359.

Vinegar, H. J. and Wellington, S. L. (1987). Tomographic imaging of threephase flow experiments. *Rev. Sci. Instrum.*, 58(1), 96–107.

Voltolini, M. and Ajo-Franklin, J. (2019). The effect of CO_2-induced dissolution on flow properties in Indiana limestone: An in situ synchrotron X-ray micro-tomography study. *Int. J. Greenh. Gas Control*, 82, 38–47.

Voltolini, M. and Ajo-Franklin, J. B. (2020). The sealing mechanisms of a fracture in opalinus clay as revealed by in situ synchrotron X-ray microtomography. *Front. Earth Sci.*, 8, article no. 207.

Voltolini, M., Barnard, H., Creux, P., and Ajo-Franklin, J. (2019). A new mini-triaxial cell for combined high-pressure and high-temperature in situ synchrotron X-ray microtomography experiments up to 400 °C and 24 MPa. *J. Synchrotron Radiat.*, 26(1), 238–243.

Voltolini, M., Haboub, A., Dou, S., Kwon, T.-H., MacDowell, A. A., Parkinson, D. Y., and Ajo-Franklin, J. (2017). The emerging role of 4D synchrotron X-ray micro-tomography for climate and fossil energy studies: five experiments showing the present capabilities at beamline 8.3.2 at the Advanced Light Source. *J. Synchrotron Radiat.*, 24, 1237–1249.

Wang, S. Y., Ayral, S., Castellana, F. S., and Gryte, C. C. (1984). Reconstruction of oil saturation distribution histories during immiscible liquid–liquid displacement by computer-assisted tomography. *AIChE J.*, 30(4), 642–646.

Wang, Y. B., Uchida, T., Westferro, F., Rivers, M. L., Nishiyama, N., Gebhardt, J., Lesher, C. E., and Sutton, S. R. (2005). High-pressure X-ray tomography microscope: Synchrotron computed microtomography at high pressure and temperature. *Rev. Sci. Instrum.*, 76(7), article no. 073709.

Wildenschild, D. and Sheppard, A. P. (2013). X-ray imaging and analysis techniques for quantifying pore-scale structure and processes in subsurface porous medium systems. *Adv. Water Resour.*, 51, 217–246.

Wildenschild, D., Vaz, C. M. P., Rivers, M. L., Rikard, D., and Christensen, B. S. B. (2002). Using X-ray computed tomography in hydrology: systems, resolutions, and limitations. *J. Hydrol.*, 267(3), 285–297.

Withers, P. J. (2007). X-ray nanotomography. *Mater. Today*, 10(12), 26–34.

Wolf, M., May, B. M., and Cabana, J. (2017). Visualization of electrochemical reactions in battery materials with X-ray microscopy and mapping. *Chem. Mater.*, 29(8), 3347–3362.

Wu, Y. X. et al. (2011). Geophysical monitoring and reactive transport modeling of ureolytically-driven calcium carbonate precipitation. *Geochem. Trans.*, 12, article no. 7.

Xing, T., Zhu, W., Fusseis, F., and Lisabeth, H. (2018). Generating porosity during olivine carbonation via dissolution channels and expansion cracks. *Solid Earth*, 9(4), 879–896.

Yang, J., Hazlett, L., Landauer, A., and Franck, C. (2020a). Augmented lagrangian digital volume correlation (aldvc). *Exp. Mech.*, 60(9), 1205–1223.

Yang, Y. et al. (2020b). Dynamic pore-scale dissolution by CO_2-saturated brine in carbonates: Impact of homogeneous versus fractured versus vuggy pore structure. *Water Resour. Res.*, 59, article no. e2019WR026112.

Yu, T., Wang, Y., and Rivers, M. L. (2016). Imaging in 3D under pressure: a decade of high-pressure X-ray microtomography development at GSECARS. *Prog. Earth Planet. Sci.*, 3(1), 1–13.

Yuan, K., Starchenko, V., Lee, S. S., De Andrade, V., Gursoy, D., Sturchio, N. C., and Fenter, P. (2019). Mapping three-dimensional dissolution rates of calcite microcrystals: Effects of surface curvature and dissolved metal ions. *ACS Earth Space Chem.*, 3, 833–843.

Yuan, K., Starchenko, V., Rampal, N., Yang, F., Yang, X., Xiao, X., Lee, W.-K., and Stack, A. G. (2021). Opposing effects of impurity ion Sr^{2+} on the heterogeneous nucleation and growth of barite ($BaSO_4$). *Cryst. Growth Des.*, 21(10), 5828–5839.

Zhao, Q., Tisato, N., and Grasselli, G. (2017). Rotary

shear experiments under X-ray micro-computed tomography. *Rev. Sci. Instrum.*, 88(1), article no. 015110.

Zheng, X., Cordonnier, B., Zhu, W., Renard, F., and Jamtveit, B. (2017). Effects of confinement on reaction-induced fracturing during hydration of periclase. *Geochem. Geophys. Geosyst.*, 19(8), 2661–2672.

Zhu, W., Fusseis, F., Lisabeth, H., Xing, T., Xiao, X., De Andrade, V., and Karato, S.-i. (2016). Experimental evidence of reaction-induced fracturing during olivine carbonation. *Geophys. Res. Lett.*, 43(18), 9535–9543.

Zitová, B. and Flusser, J. (2003). Image registration methods: a survey. *Image Vis. Comput.*, 21(11), 977–1000.

Zuo, L., Ajo-Franklin, J. B., Voltolini, M., Geller, J. T., and Benson, S. M. (2017). Pore-scale multiphase flow modeling and imaging of CO_2 exsolution in sandstone. *J. Pet. Sci. Eng.*, 155, 63–77.